Tilting Pad Journal Bearing Misalignment Effect on Thermally Induced Synchronous Instability (Morton Effect)

Dongil Shin
Department of Mechanical Engineering,
Texas A&M University,
College Station, TX 77840
e-mail: davshin@tamu.edu

Alan B. Palazzolo[1]
Professor
Fellow ASME
Department of Mechanical Engineering,
Texas A&M University,
College Station, TX 77840
e-mail: a-palazzolo@tamu.edu

This paper investigates the influence of misaligned journal bearing effects on the thermally induced rotor instability (Morton effect "ME") problem. The Morton effect is caused by uneven viscous heating of the journal in a fluid film bearing, which causes thermal bending, especially in rotors with an overhung disc or coupling weight. The thermally induced bending in the shaft may cause a vibration instability, which results in an excessive level of synchronous vibration. Previous research focused on parametric studies of the rotor and bearing design parameters, including overhung mass, bearing radial clearance, and lubricant viscosity. The present study investigates the influence of journal misalignment on the Morton effect. A coupled fluid-thermal-structural, three-dimensional finite element model (FEM) is developed to simulate fluid film pressures and temperatures, and shaft temperatures and vibrations. Simulations were conducted with different ratios of journal misalignment, and different pad-pivot types to determine their effect on the phenomenon. The simulation results indicate that the amplitude of the misalignment angle affects the instability speed range (ISR) caused by the Morton effect under certain conditions.
[DOI: 10.1115/1.4048164]

Keywords: bearings, fluid film lubrication, hydrodynamic lubrication, journal bearings, thermoelastohydrodynamic lubrication

1 Introduction

Eccentric, synchronous vibrations in rotating machinery cause asymmetric temperature distribution around the circumference of the journal in a hydrodynamic bearing (HB).

This produces thermal bow in the shaft, and under some conditions increasing vibration and inevitable shutdown of the machinery. This "Morton effect" (ME) is becoming increasingly observed due to the higher performance requirements of modern machinery and the increasing use of a HB [1]. The ME is the nonlinear synchronous vibration induced by differential viscous shearing of the HB's lubricant, which gives rise to hot and cold spots on the journal circumference. This increased bow, in particular with overhung rotors, results in larger inertial force and more heating induced by viscous shearing. The viscous shearing, the thermal bow, and the inertial force may form a positive feedback loop, driving the rotor system into a limit cycle vibration, or rubbing between the journal and bearing bushing.

The ME instability phenomenon is highly sensitive to operating and physical parameters [1]. Therefore, even minor changes in parameters and conditions may suppress or induce the ME in the machine. This explains why only a single machine may experience the ME, while other "identical" machines operate free from the ME. The axial film thickness asymmetry due to journal misalignment is prevalent in turbomachinery systems due to inevitable installation/manufacturing errors and deflections/distortions caused by applied loads. Therefore, there is a need for the present investigation of the effect of bearing misalignment on the ME, given its known sensitivity to parameter variations.

de Jongh and Van Der Hoeven [2] reported an experimental ME case of an overhung rotor showing high vibration levels due to a thermal instability caused by journal differential heating. The instability problem was mitigated by installing a heat barrier sleeve to prevent the heat input into the shaft. Keogh and Morton [3] modeled the journal differential heating with a short bearing theory, iso-viscous, thermohydrodynamic (THD) model. Lee and Palazzolo [4] developed a ME model based on a variable viscosity Reynolds equation, a two-dimensional energy equation, and a heat conduction equation. Long time constant, cyclically varying, large amplitude vibration caused by asymmetric journal heating is predicted, using a transient simulation method. Suh and Palazzolo [5–8] developed the first high-fidelity ME prediction model utilizing finite length, three-dimensional (3D) thermo-elasto-hydrodynamic tilting pad journal bearing (TPJB) models and performed parametric studies. Tong et al. [9] and Tong and Palazzolo [9–11] further expanded the high-fidelity ME model to include distributed thermal bow and a double overhung type rotor configuration. The same authors measured journal circumferential temperature distributions and verified the accuracy of the high-fidelity model, compared with simplified prediction models in Ref. [12]. The same authors theoretically showed that the ME can be induced in a gas bearing supported machinery in Ref. [13].

Misalignment effects on HB have been investigated in many research studies. Bouyer and Fillon [14] presented experimental results for a misaligned plain journal bearing. Their measurements at the bearing mid-plane showed the bearing performance, i.e., maximum pressure, temperature distribution, oil flowrate, and minimum film thickness was significantly affected by misalignment. Sun and Gui [15] showed that shaft deformation-induced bearing misalignment had a significant effect on bearing performance.

El-Butch and Ashour [16] proposed an improved fidelity, TPJB, THD model with journal misalignment and pad elastic/thermal distortion effects, which was solved with transient simulation. Sun et al. [17] showed that thermal and surface roughness effects play a vital role in the performance predictions for a misaligned journal bearing, especially for large eccentricity ratios. Xu et al.

[1]Corresponding author.

Contributed by the Tribology Division of ASME for publication in the JOURNAL OF TRIBOLOGY. Manuscript received August 20, 2019; final manuscript received August 5, 2020; published online September 21, 2020. Assoc. Editor: Daejong Kim.

[18] showed that misalignment significantly affects journal bearing performance at large eccentricity ratios, utilizing a THD model. Suh and Choi [19] presented a study on the combined effects of misalignment and tilting pad journal bearing pivot type on static performance. Their theoretical study showed that spherical pivots having tilting, pad yaw, and rolling motions compensates misalignment effects.

The present study reveals a marked dependence of the ME on tilting pad journal bearing misalignment. This is established utilizing a high-fidelity model described with 3D THD models of the fluid film, and 3D solid FEM bearing, and shaft structure models discussed in Sec. 2. The journal misalignment model is included in the high-fidelity bearing model, and the influence of its asymmetric fluid film distribution on the ME occurrence is investigated. The impact of pad-pivot type on the ME, with journal misalignment, is also considered.

2 Modeling and Morton Effect Prediction Algorithms

2.1 Tilting Pad Journal Bearings. The Reynolds equation for an incompressible Newtonian fluid with variable fluid viscosity and negligible fluid inertia/shaft curvature is

$$\nabla \cdot (C_1 \nabla P) + \nabla D_2 \cdot U + \partial h/\partial t = 0 \tag{1}$$

where C_1 and C_2 are constants related to variable viscosity μ

$$C_1 = \int_0^h \int_0^z (\xi/\mu) d\xi dz - C_2 \int_0^h (\xi/\mu) d\xi,$$
$$C_2 = \int_0^h \int_0^z (1/\mu) d\xi dz / \int_0^h (1/\mu) d\xi$$

where z is the axial coordinate of the fluid film bearing. This form assumes laminar flow, uniform pressure distribution in the direction of film thickness, constant fluid density, and temperature-dependent variable viscosity. The viscosity–temperature relation is

$$\mu = \mu_0 e^{-\alpha(T-T_0)} \tag{2}$$

where α is the coefficient of viscosity, and μ_0 and T_0 are the reference viscosity and temperature, respectively. The fluid film temperature T is solved for with the energy equation which is coupled with the Reynolds equation through the viscosity and velocity terms. The pressure distribution obtained from the Reynolds equation is utilized to obtain the fluid velocity from the relation

$$u = \left(\int_0^z (\xi/\mu) d\xi - \int_0^h (\xi/\mu) d\xi \frac{\int_0^h (1/\mu) d\xi}{\int_0^h (1/\mu) d\xi} \right) \nabla p + \frac{\int_0^z (1/\mu) d\xi}{\int_0^h (1/\mu) d\xi} U \tag{3}$$

The ∇p term is calculated in both the circumferential and axial directions for a full 3D thermo-hydrodynamic analysis. The Reynolds cavitation model, which imposes a zero-pressure gradient at the cavitation boundary is utilized in the Morton effect simulations. This approach is widely utilized in the literature about journal misalignment [19–22]. Moreover, significant thermal expansion of the shaft and bearing pad accompanies the Morton effect. This decreases the film thickness significantly, which tends to suppress cavitation, as evidenced in the simulation results. Of course, more sophisticated, and more computationally intensive, cavitation models can be applied. This will be done in future work.

The two types of pad-pivots studied are cylindrical and spherical. The cylindrical pivot has angular pad tilting (pitch), and translational pivot motion (deformation), and the spherical pivot has rolling and yawing motions in addition to those of the cylindrical pivot. The model for journal and pad dynamics is illustrated in Fig. 1(*a*).

The film thickness formula for the spherical- type pivot TPJB is

$$h(\theta, z) = C_P - \hat{e}_x \cos(\theta) - \hat{e}_y \sin(\theta) - (C_P - C_b)\cos(\theta - \theta_P) - \delta_{tilt} R \sin(\theta - \theta_P) - h_{shaft.TE}(\theta, z) - h_{pad.TE}(h, z) \tag{4}$$

where

$$\hat{e}_x = e_x - y_{pvt} \cos\theta_p - z\alpha_{roll} \cos\theta_p - z\beta_{yaw} \cos(\theta_p + \pi/2),$$
$$\hat{e}_y = e_y - y_{pvt} \sin\theta_p - z\alpha_{roll} \sin\theta_p - z\beta_{yaw} \sin(\theta_p + \pi/2)$$

and

- C_P and C_b represent pad and bearing radial clearances.
- y_{pvt}, δ_{tilt}, α_{roll}, β_{yaw} are the pad-pivot deformation, and tilting, rolling and yawing pad angular displacements, respectively.
- z and R are the axial position and the journal radius, respectively.
- θ and θ_p are the circumferential coordinate of the bearing and pivot circumferential positions, respectively, as shown in Fig. 1(*a*).

Equation (4) considers the journal/bearing pad's asymmetric thermal expansion, the variation of axial and circumferential motions of pads, and deformation due to pivot compliance. The terms $h_{shaft.TE}$ and $h_{pad.TE}$ in Eq. (4) are the thermal expansions of the shaft and pads as illustrated in Fig. 1(*b*). For the cylindrical pivot-type model, the terms related to roll α_{roll} and yaw β_{yaw} motions are removed from the equation.

Journal misalignment is an imposed shift in angular position of the bearing or shaft. The misalignment term is incorporated into Eq. (4) by adding the terms α_x and α_y which represent the journal angular displacements in the $x - z$ and $y - z$ planes, respectively, as illustrated for α_y in Fig. 2.

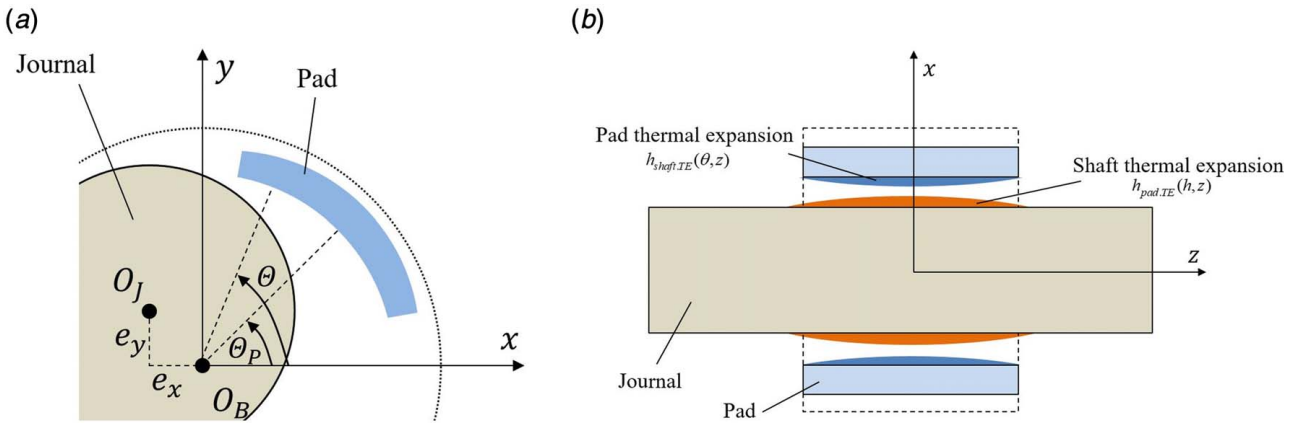

Fig. 1 (*a*) Model for journal dynamics and (*b*) thermal expansion of pad/shaft

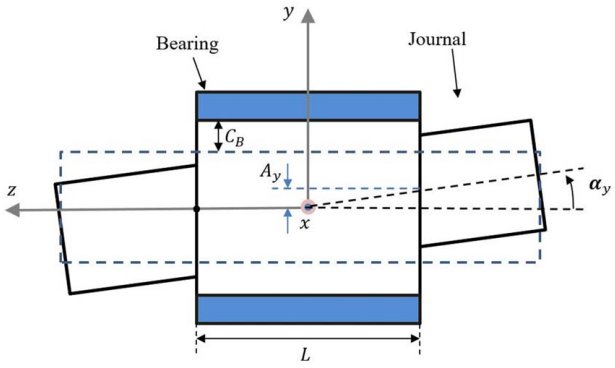

Fig. 2 Permanent misalignment angle α_y

The misalignment ratio, misalignment angle, and misalignment phase are defined as

$$r_y = \frac{A_y}{C_B}, \quad r_x = \frac{A_x}{C_B}$$
$$\alpha_y = A_y \frac{2}{L}, \quad \alpha_x = A_x \frac{2}{L} \tag{5}$$
$$r_\alpha = \tan^{-1} \frac{\alpha_y}{\alpha_x}$$

where A_y is the journal/bearing relative, end displacement due to α_y, and C_B and L are the bearing radial clearance and length. The misalignment ratio and angle α_x in the $x-z$ plane have similar definitions. For characteristically small misalignment angles, $\sin \alpha_y = \alpha_y$ applies. Then the updated equations for $\hat{e}_x$ and $\hat{e}_y$ with the misalignment terms become

$$\hat{e}_x = e_x - y_{pvt} \cos\theta_p - z\alpha_{pitch} \cos\theta_p - z\beta_{yaw} \cos(\theta_p + \pi/2) + z\alpha_x$$

$$\hat{e}_y = e_y - y_{pvt} \sin\theta_p - z\alpha_{pitch} \sin\theta_p - z\beta_{yaw} \sin(\theta_p + \pi/2) + z\alpha_y \tag{6}$$

Two configurations of misalignment, i.e., $r_\alpha = 90$ deg and 270 deg are illustrated in Fig. 3 to explain the misalignment phase. Note that the right side of the shaft in the figure is the non-drive end (NDE) side, while the other side is the drive end (DE). For both configurations, the misalignment ratio in the x direction is zero ($r_x = 0$). If the r_y value is nonzero and positive, the misalignment angle will be 90 deg from Eq. (5), and it corresponds to the case in Fig. 3(*a*).

The 270 deg misalignment angle case in Fig. 3(*b*) has the same magnitude of misalignment ratio as the 90 deg case but with opposite sign, and this makes the misalignment phase of this case equal to −90 deg (= 270 deg) based on Eq. (5).

The equations for the tilting pad journal bearing with spherical pivot-type pads in Fig. 4 with small motions are [19]

$$M_{pad\_i} \ddot{y}_{pvt} = -K_P y_{pvt} + F_{pad\_i}$$

$$I_{tilt\_i} \ddot{\delta}_{tilt} = MO_{tilt\_i}$$

$$I_{roll\_i} \ddot{\alpha}_{roll} = MO_{roll\_i}$$

$$I_{Yaw\_i} \ddot{\beta}_{yaw} = MO_{yaw\_i} \tag{7}$$

where i represent the number of pads, M_{pad_i}, I_{tilt_i}, I_{roll_i}, and I_{Yaw_i} are the mass and the tilting/rolling /yawing inertias of each pad, respectively, and F_{pad_i}, MO_{tilt_i}, MO_{pitch_i}, and MO_{yaw_i} represent the fluid film force and the tilting/rolling/yawing moments

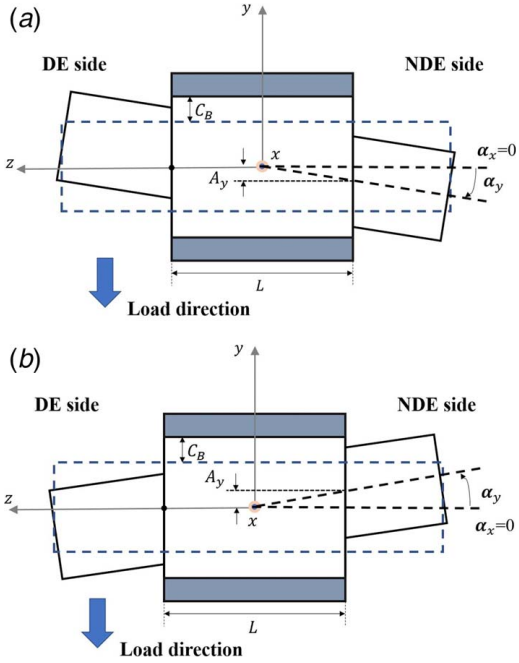

Fig. 3 Configuration of journal misalignment phase directions: (*a*) $r_\alpha = 90$ deg and (*b*) $r_\alpha = 270$ deg

applied to a pad, respectively. The equations can be applied to a cylindrical pivot-type tilting pad journal bearing by removing the rolling and yawing motions from Eq. (7).

2.2 Thermal Model—Three-Dimensional Energy Equation. The energy equation

$$\rho c \left(u\frac{\partial T}{\partial x} + w\frac{\partial T}{\partial z} \right) = k\left(\frac{\partial^2 T}{\partial x^2} + \frac{\partial^2 T}{\partial y^2} + \frac{\partial^2 T}{\partial z^2} \right) + \mu \left[\left(\frac{\partial u}{\partial y} \right)^2 + \left(\frac{\partial w}{\partial y} \right)^2 \right] \tag{8}$$

is solved utilizing eight-node isoparametric finite elements to obtain the 3D temperature distribution T across the fluid film. The quantities in (8) are the film temperature T, density ρ, specific heat capacity c, thermal conductivity k, circumferential velocity u, and axial velocity v. The convection term in the film thickness direction is not considered due to the assumed thin film (bearing radial

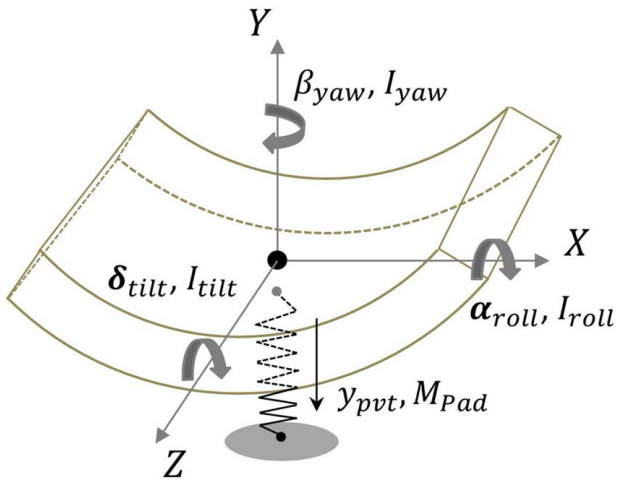

Fig. 4 Spherical pad-pivot-type tilting pad dynamic model

clearance 68 μm, bearing radius 40 mm) while the conduction term is considered in all x, y, and z directions. This approach is commonly used in the literature [23–25]. The fluid film temperature T is obtained during each journal orbit by solving Eq. (8) using the variable viscosity μ relation in Eq. (2), as discussed in Sec. 3. The pad inlet boundary temperature is obtained from the mixing theory in Ref. [5]. An up-winding scheme [26] is used in the finite element solution of Eq. (8) to avoid spatial oscillations due to the convective term. The film temperature is modeled as a quasi-steady-state problem.

Shaft and pad temperatures are predicted with the Laplace equation

$$\frac{\partial^2 T}{\partial x^2}+\frac{\partial^2 T}{\partial y^2}+\frac{\partial^2 T}{\partial z^2}=\frac{\rho c}{k}\frac{\partial T}{\partial t} \tag{9}$$

assuming constant thermal conductivity. Utilizing 3D eight-node isoparametric FEM, the discrete form of (9), i.e.,

$$[C][\dot{T}]+[K][T]=0 \tag{10}$$

The transient solution of Eq. (10) is obtained via numerical integration. The solid finite element, thermal model extends seven times the journal length, either side of the journal, in the present model. This is based on simulations that showed little change in temperatures incurred by larger extensions. Of course, the extension lengths could be varied in actual applications. Convection to ambient atmosphere is assumed to occur outside of the journal.

2.3 Thermal Deformation of the Shaft and Bearing. The hybrid finite element model (HFEM) shown in Fig. 5 is used to determine deformations resulting from the asymmetric temperatures in the journal and adjacent rotor segments while exploiting the computational efficiency of beam finite elements.

The solid finite element model extends seven times the journal length in the present model based on simulations that showed little change incurred by larger extensions. Of course, the extension lengths could be varied in actual applications. Thermal deformations of the shaft and bearing are obtained from discrete FE equation of the form

$$[K_{\Delta T}][D_{\Delta T}]=[F_{\Delta T}] \tag{11}$$

where $D_{\Delta T}$ is the nodal displacement vector in x, y, and z directions induced by the thermal load vector $F_{\Delta T}$ which is obtained from the temperature fields determined from Eq. (10). Details of the thermal bow calculation utilizing the HFEM are provided in Ref. [9]. The thermal bow is calculated in the rotating reference frame and becomes a dynamic force in the stationary frame equations of motion.

2.4 Thermal Boundary Conditions on the Shaft and Pads. Thermal boundary conditions are applied at interfaces between the fluid (lubricant) and structures (bearing pad and journal), and between the shaft and atmosphere as shown in Fig. 6.

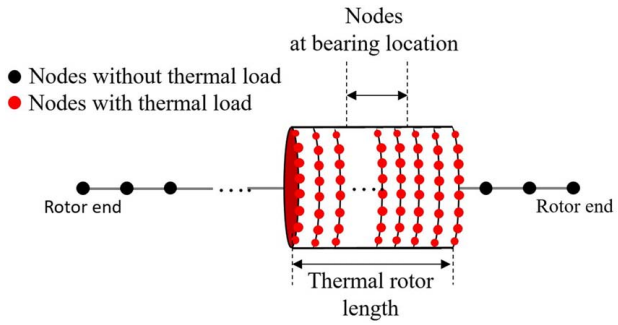

Fig. 5 Diagram illustrating the HFEM rotor structural model

Heat flux and temperature boundary conditions are imposed at the interface between the lubricant and pad

$$k_L\left.\frac{\partial T_L}{\partial r}\right|_{r=R+H}=k_B\left.\frac{\partial T_B}{\partial r}\right|_{r=R+H}$$

$$T_L|_{r=R+H}=T_B|_{r=R+H} \tag{12}$$

The heat flux and temperature boundary conditions at the lubricant–journal interface are

$$k_L\left.\frac{\partial T_L}{\partial r}\right|_{\theta=0,r=R}=k_J\left.\frac{\partial T_J}{\partial r}\right|_{\theta=-\omega t,r=R}$$

$$T_L|_{\theta=0,r=R}=T_J|_{\theta=-\omega t,r=R} \tag{13}$$

These conditions must be applied in the rotating frame for the journal mesh which is continuously re-oriented during the time transient simulation. Thermal boundary conditions are applied at the following surfaces in Fig. 6; two bearing pad side surfaces, one bearing pad surface, two shaft side surfaces, and two journal surfaces.

2.5 Rotor Dynamic Model. Lateral dynamics utilizes Euler beam elements, and modal reduction is used for computational efficiency. The system equations of motion are

$$[\dot{U}]=[D][U]+[F] \tag{14}$$

where $[U]=\begin{bmatrix}\dot{Z}\\ Z\end{bmatrix}$, $[D]=\begin{bmatrix}-M_{ro}^{-1}C_{ro} & -M_{ro}^{-1}K_{ro}\\ 1 & 0\end{bmatrix}$, $[F]=\begin{bmatrix}M_{ro}^{-1}F_{ro}\\ 0\end{bmatrix}$. U, M_{ro}, C_{ro}, and K_{ro} are the state vector and mass, damping and stiffness matrices of the rotor, F_{ro} is the force vector including the nonlinear fluidic forces from the bearings, imbalance forces, forces induced by thermal bow and gravity, etc.

Equation (14) is diagonalized utilizing biorthogonality with the right eigenvector ψ_R and left eigenvector ψ_L of the matrix $[D]$. Equation (14) becomes

$$[\dot{Y}]=[A][Y]+[\psi_L^T][F] \tag{15}$$

where $[Y]=[\psi_R][U]$, $[A]=[\psi_{Lm}^T][D][\psi_{Rm}]=\begin{cases}\lambda_i & m=n\\ 0 & m\neq n\end{cases}$. λ_i is the ith eigenvalue of the system. Modes five times larger than spin speed are ignored to reduce the computational complexity. Equations (7) and (15) are solved simultaneously with numerical integration.

3 Morton Effect Computation Algorithm

The diagram describing the ME transient simulation algorithm is presented in Fig. 7. The initial conditions of the rotor-bearing state variables, lubricant/shaft/bearing pad temperature distribution, and thermal expansion and bow states are specified at the start of the simulation. To perform (1) the transient rotor and TPJB dynamics are solved by numerical integration, until the rotor orbits converge to steady state, utilizing the rotor-bearing dynamic equations in Eq. (7) and (15) with the film thickness and journal misalignment formulae in Eqs. (4),(5), and (6), the Reynolds equation in Eq. (1) and the energy equation in Eq. (8). The fluid velocities from Eq. (3) are obtained from the Reynolds equation and are used in the energy equation solution. Each journal orbit is both temporally and spatially divided into N steps as illustrated in Fig. 7. The energy equation is solved at the end of each of the N steps, in order to (1) obtain the orbit-averaged lubricant temperature and the flux boundary conditions of fluid–structure interfaces (lubricant/bearing and lubricant/journal) and to (2) update the variable

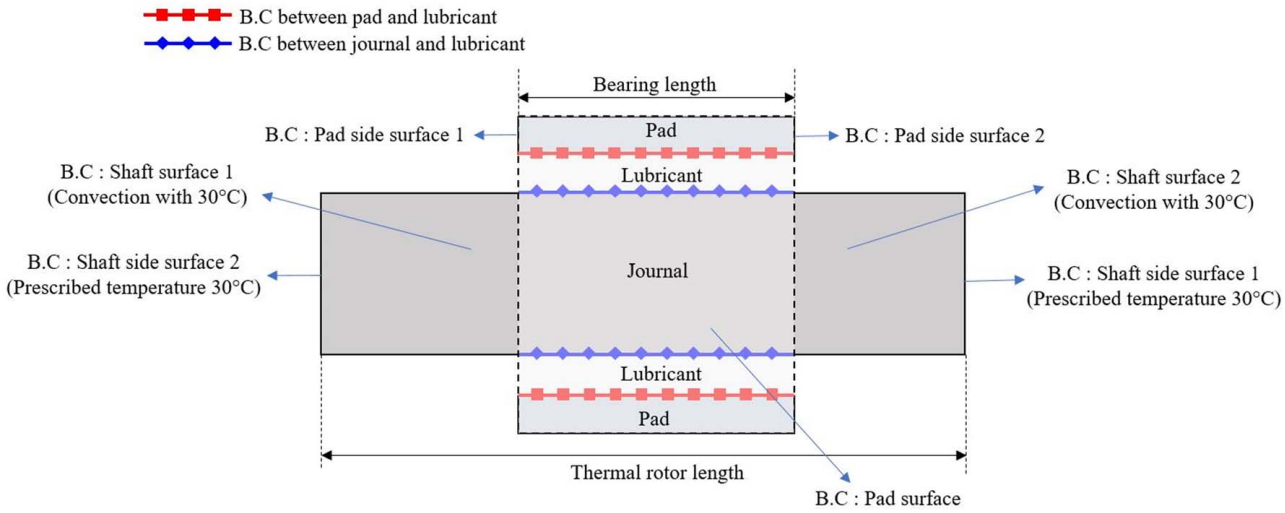

Fig. 6 Thermal boundary conditions on rotor and bearing surfaces

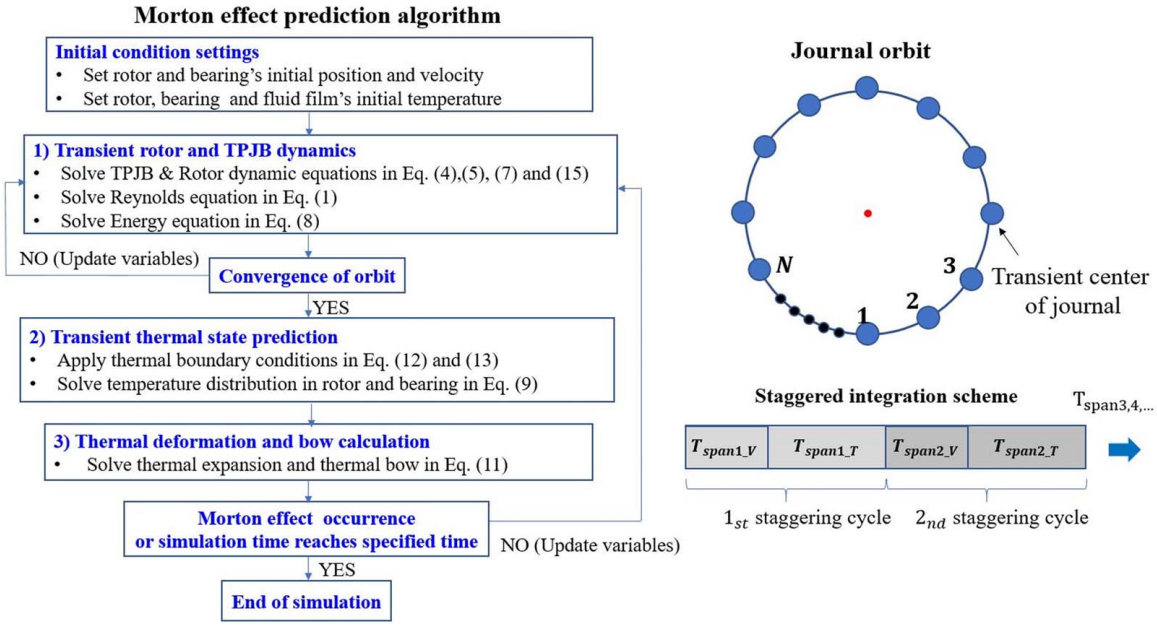

Fig. 7 Algorithm for Morton effect transient simulation

viscosity in Eq. (2). Then the Reynolds equation, combined with the dynamic equations, is also solved at every orbit segment with the updated variable viscosity from the previous step. Once the orbit of journal converges to its steady state, the (2) transient thermal state predictions for the shaft and bearing pads are completed based on the lubricant temperature distribution and flux boundary conditions obtained in the previous step (1). The prescribed convective thermal boundary conditions on the shaft and bearing pad outer surfaces, and the lubricant's thermal states obtained at the journal/lubricant and lubricant/bearing pad interfaces in Eqs. (12) and (13) provide the thermal boundary conditions for solving the shaft/bearing pad conduction problems Eq. (9).

The thermal expansions of shaft/bearing pads and the thermal bow amplitudes of the shaft are calculated based on Eq. (11) in step 3. All steps in (1)–(3) will be repeated until the ME instability criteria discussed in Sec. 4 are met, or until the limit time is reached. Updated variables are utilized in this process, including the fluid and structural temperature distributions, the new film thickness reflecting the calculated thermal expansion of the shaft and pads, the thermal bow of the shaft, the lubricant viscosity, and the thermal boundary conditions on shaft/pads.

The rotordynamic structural states change with extremely short time constants compared with the thermal variable time constants. Thus integrating both problems with the same numerical integration time-step is computationally impractical and unnecessary, and the staggered–time-integration technique in Fig. 7 is applied. In the 1_{st} stagger cycle, the rotordynamic equations including the rotor and bearing structures are numerically integrated with the time-step of T_{span1_V}, with invariant rotor and bearing temperatures/deformations/bow during the one orbit period. Next, the temperature distributions of the structures are calculated with the larger time constant of T_{span2_V}, while the rotor/bearing motion states are held invariant. The use of different time-steps in T_{span1_V} and T_{span2_V} is justified due to the much slower heat transfer process compared with the rotordynamic motions. A quicker simulation is achieved without overly sacrificing accuracy. Heat flux and temperature continuity

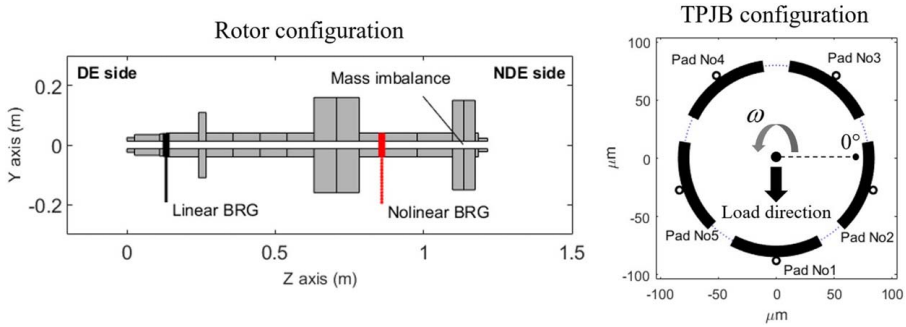

Fig. 8 Example rotor-bearing configuration

at the film–solid interfaces are explicitly enforced at all simulation times in our model. In particular, this is performed in the staggered time approach, where the shaft orbit is constant during the thermal solution update.

For the steady-state transient simulation, the transient simulation explained above starts from the lowest speed of interest and simulates the rotor-bearing system response until either steady-state or an unacceptable vibration level (caused by the ME) occurs. Then, the process stops and repeats the simulation at the next higher speed. Steady-state occurs if the errors between the temperature and dynamics states of the entire rotor-bearing system at the previous time-step, and at the current time-step, are less than the specified error criteria. The final temperature/dynamic states of the previous speed are transferred to the initial conditions for the next speed to improve the computational efficiency of the process. When the unstable rotor response is detected, the initial states of the next speed is determined by the average of the final state of the previous step, and the initial states of the highest operating speed just below the instability onset speed (IOS).

The linear method [10] provides an alternative approach and estimates stiffness and damping coefficients of the bearings and combines them into the rotor matrix to formulate the system matrix. The rotor-bearing dynamic response is calculated at different operating speeds instead of calculating the bearing hydrodynamic forces at each time-step as in the nonlinear transient method. The linear method calculates the lubricant temperature and variable viscosity at each orbit segment. However, this method is inherently inaccurate compared with the nonlinear transient method because (1) the responses determined utilizing the dynamic coefficients calculated at the journal equilibrium position become inaccurate when the orbit size becomes large and (2) the linear method neglects the inertial forces resulting from the thermal bow caused by the viscous heating.

4 Simulation Results

Figure 8 shows a single overhung, example rotor with a linear bearing (node 4) at the drive end DE side and a nonlinear bearing (node 13) at the NDE side. A mass imbalance is located at node 16 along with the NDE overhung mass of 40 kg. The TPJB at the NDE side has five tilting pads with a load-on-pad configuration as shown in Fig. 8. The parameters of the example rotor-bearing configuration are listed in Table 1. The thermal boundary conditions illustrated in Fig. 6 are applied on the rotor and the bearing pad surfaces with a convection coefficient of 50 W/m^{2}K and the ambient temperature of 30 °C. These parameter values are utilized for all simulations except for the Rotor 2 case in Sec. 4, which has an increased bearing radial clearance, compared with that of the original rotor. A case was run with the rotor convection coefficient equal to 250 W/m^{2}K outside the bearing, and the results showed no influence on the predicted response with the Morton effect. Therefore, all cases utilized 50 W/m^{2}K. The Rotor 1 case is defined with the original parameter values as shown in Table 1. The mesh sizes of the FEM are $40\times7\times17$ (circumferential, radial, and axial directions) for both the thermal and temperature predictions, $15\times7\times7$ for the lubricant film and $15\times8\times8$ for the energy equation solvers, and the numerical tolerances of the MATLAB ordinary differential equations (ODE) solver are selected as $1e^{-5}$ for absolute and $1e^{-4}$ for relative, respectively. A convergence test was performed with three times the current mesh size, and with tolerances of

Table 1 Parameter values for the example system

Lubricant parameters		*Bearing parameters*	
Viscosity at 50 (Ns/m^2)	0.0203	Pad type	Load on pad
Viscosity coefficients (1/°C)	0.031	No. of pads	5
Supply temperature (°C)	50	Radius of shaft (m)	0.04
Inlet pressure (Pa)	1.32×10^5	Bearing clearance (C_b) (m)	6.8×10^{-5}
Reference temperature (°C)	50	Preload	0.25
Rotor parameters		Bearing length (m)	0.06
Heat capacity (J/kg °C)	453.6	Thermal expansion coefficient (1/°C)	1.1×10^{-5}
Heat conductivity (W/mK)	50	Reference temperature (°C)	30
Thermal expansion coefficient (1/°C)	1.22×10^{-5}	Pad-pivot stiffness (N/m)	4e8
Reference temperature (°C)	25	Pivot offset	0.5
Rotor length (m)	1.214	*Linear bearing*	
Rotor inner diameter (m)	0.0254	Kxx, Kyy (N/m)	1.7×10^8
Rotor outer diameter (m)	0.08	Cxx, Cyy (Ns/m)	1.0×10^5
Mass of wheel 1 (kg)	6.43	*Thermal boundary conditions*	
Mass of wheel 2 (kg)	90	Temperature on shaft surface (°C)	30
Mass of overhung wheel (kg)	40	Temperature on bearing surface (°C)	30
Initial(mechanical) imbalance (kg m)	6.5e−5	Convection coefficient (W/m^{2}K)	50
		Thermal rotor length (m)	0.18

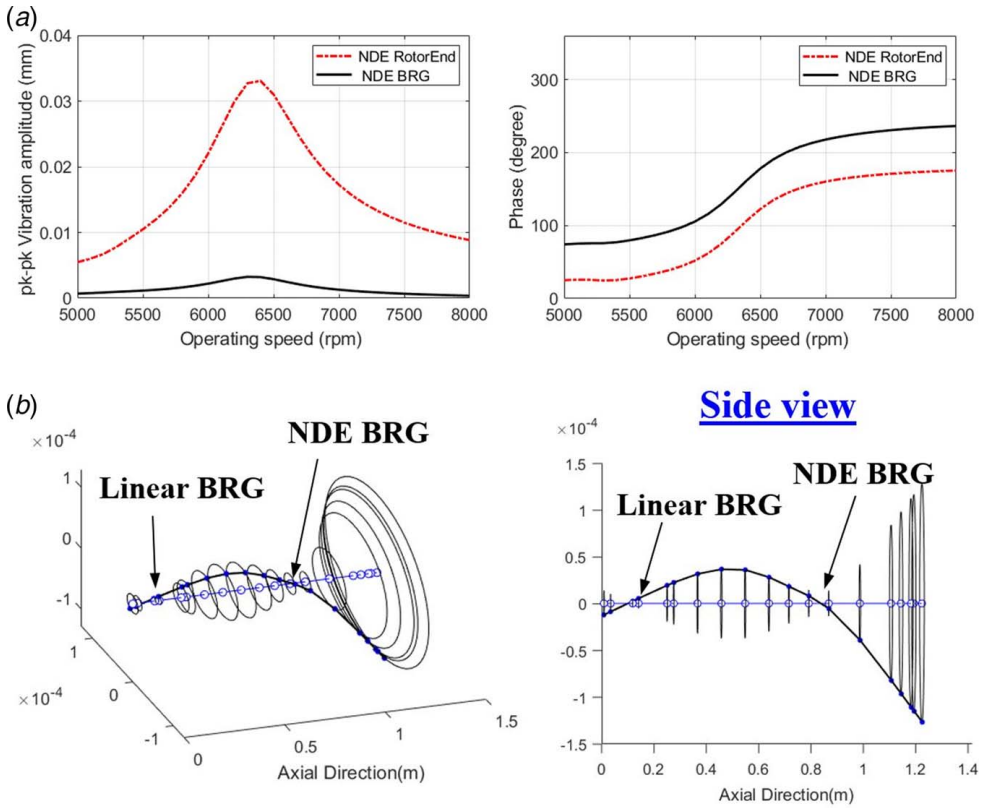

Fig. 9 Rotor 1: (*a*) Imbalance response amplitude and phase lag and (*b*) mode shape of the third critical speed at 6343 rpm

$1e^{-7}$ and $1e^{-6}$, and the results showed quite similar results with the presented predictions.

The ME is a fully nonlinear phenomenon producing a synchronous 1× instability, as compared with typical linear instability resulting from positive real part eigenvalues. A ME instability is defined here as when the rotor vibration and journal ΔT increases abruptly, and the minimum film thickness drops below 10% of C_b at constant operating speed, while the corresponding system without ME has acceptable vibration and minimum film thickness levels. A linear analysis is conducted to identify the critical speeds, mode shapes, damped unbalance response, and damping ratio of the system as shown in Fig. 9. The linear analysis result is included solely for comparison with the ME response and is obtained from conventional rotodynamic analysis. The linearized bearing coefficients are obtained from a THD model which includes solutions for temperature and viscosity distributions by solving the energy equations in the film and bearings. The ME thermal bow effect is not included. This utilizes the Rotor 1 bearing's linearized damping and stiffness coefficients as explained in Sec. 3, neglects bearing misalignment, and utilizes a constant imbalance for all speeds. Figure 9(*a*) shows a large vibration level near the rotor's third critical speed of 6343 rpm, with corresponding damping ratio 0.05 detected at both the NDE bearing and rotor end locations. Figure 9(*b*) shows that overhung disc modal displacement are significantly larger than the corresponding bearing components, in the bending (critical speed) mode at 6343 rpm.

Case histories of the ME [2,3] showed ME instability near the bending critical speeds of the rotor. The journal ΔT (temperature differential across a journal diameter) is the root cause of the thermal bow and is induced by synchronous rotor vibration, which typically peaks at a critical speed. Prior ME studies [11] revealed that larger imbalance force induces larger orbit size, and journal ΔT. Machines operating near the bending critical speed typically amplify synchronous vibration of the rotor, which could lead to increased journal ΔT, and resultant thermal bow. Then, the thermal deflection will more dramatically increase with an overhung bending mode shape, compared with other mode shapes, even with identical values of journal ΔT [11].

Figure 10 shows the effect of bearing misalignment on linear unbalance response amplitude. The applied misalignment ratios are $r_x = 0$ and $r_y = 0.3$, respectively, which correspond to a misalignment phase of 90 deg from Eq. (5). Based on Eq. (5), and the bearing parameters in Table 1, the $r_m = \sqrt{r_x^2 + r_y^2} = 0.3$ misalignment ratio results in a misalignment angle of $\alpha_y = 0.00086$ rad and resultant misalignment displacement $A_y = 0.0258$ mm. Figure 10 shows the vibration amplitudes at the NDE bearing location and the rotor end increase slightly with bearing misalignment. The

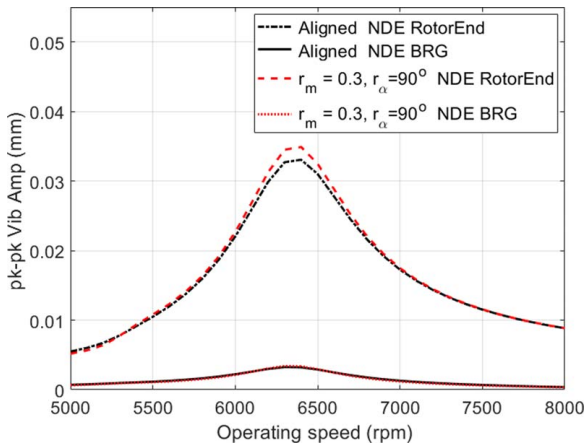

Fig. 10 Rotor 1's damped unbalance responses for aligned and misaligned cases

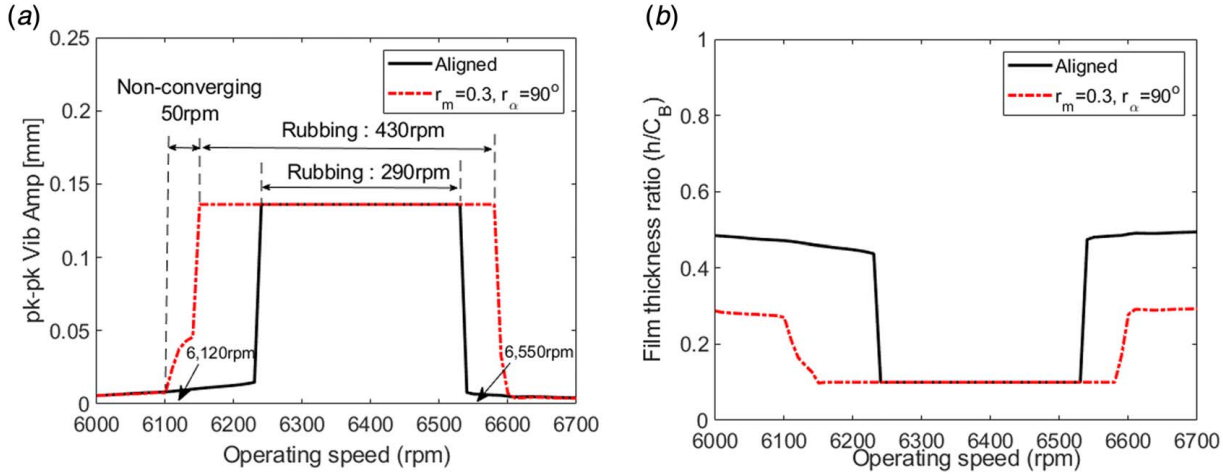

Fig. 11 Comparison of Rotor 1: (*a*) pk-pk vibration at the NDE bearing position and (*b*) minimum film thickness ratio

critical speeds are almost identical with 6343 rpm for the aligned journal and 6346 rpm for the misaligned journal. The increments of vibration level between the aligned and misaligned cases at 6343 rpm are 0.000146 mm at the NDE bearing, and 0.0183 mm at the rotor end, respectively. The damping ratios of the aligned and misaligned cases are quite similar with 0.05 and 0.0466, respectively. With the slightly smaller damping ratio for with-misalignment, the misaligned rotor's vibration amplitude shows a slightly increased vibration amplitude.

Both bearing clearance and misalignment were varied to investigate their influences on the ME utilizing the nonlinear transient model. The rotor with parameters in Table 1 is referred to as Rotor 1, and an identical rotor with increased bearing radial clearance is referred to as Rotor 2.

Steady-state simulations, using the nonlinear transient model explained in Sec. 3, were conducted with aligned and misaligned journals at various speeds. The operating speed is varied from 6000 rpm to 6700 rpm with a speed increment of 10 rpm.

Steady-state transient simulation results for the Rotor 1 case (original parameters) are presented in Figs. 11 and 12. Figure 11(*a*) shows the NDE bearing location pk-pk vibration amplitude. For the misaligned journal case, the misalignment ratios are $r_x = 0$ and $r_y = 0.3$, corresponding to 90 deg of misalignment phase as shown in Fig. 3. ME instability speed ranges (ISRs) for the aligned and misaligned cases are shown. The simulation terminates if the journal motion reduces the minimum film thickness below 10% of the bearing clearance, since this clearly establishes the occurrence of a severe Morton effect event, with vibration levels far exceeding API recommended shutdown levels. This high vibration is indicative of a near rub condition, however the simulation is terminated before rub actually occurs. The IOS is identified as the operating speed where vibration level abruptly increases. The misaligned journal exhibits the IOS at 6150 rpm which is 90 rpm lower than the aligned case (6240 rpm).

The pk-pk vibration of the misaligned journal shows an acceptable level above 6580 rpm. The ISR of the misaligned case is 430 rpm (6150 rpm–6580 rpm) over the operating speed range (6000 rpm–6700 rpm) while the ISR of the aligned journal is 310 rpm (from 6240 rpm to 6530 rpm). This shows that the machine with the misaligned journal may experience ME instability at lower speeds and that the unstable vibration is sustained over a wider speed range compared with the aligned case. The misaligned case also shows a speed range where ME instability occurs but not converge or lead to an unacceptable vibration level, as illustrated between 6100 and 6150 rpm in Fig. 11. Comparison of Figs. 10 and 11 show that although misalignment has a significant influence on the ME IOS, it has little influence on the critical speed. This stands in contrast to changing other parameters such as lubricant viscosity/temperature, bearing clearance, and overhung mass, which shift the IOS and significantly change the critical speed [11].

Figure 11(*b*) shows the minimum film thickness ratio for the aligned and misaligned cases. The ISR which corresponds to where the minimum film thickness ratio is 10% of C_b is seen to be identical to the range of large pk-pk vibration in Fig. 11(*a*). It is notable that the minimum film thickness ratios of the misaligned case are less than those of the aligned case in all speed ranges. The decreased minimum film thickness ratio is attributed to the displacements of the journal in the journal misalignment direction. In the linear analysis in Fig. 10, the damped unbalance response and damping ratio of the aligned and misaligned cases showed quite similar results, indicating no significant vibration level change in the presence of the misalignment. Unlike the linear analysis of Fig. 10, the nonlinear transient simulation revealed significant ME related vibration is only present in the misaligned journal case at specific speed ranges. This is explained by the induced hot/cold spots and thermal bow effect caused by the decreased minimum film thickness, which can be only captured in the nonlinear transient simulation.

Figure 12(*a*) shows the peak journal ΔT across the journal diameter versus the rotor axial position and the rpm. Only rotor axial positions ranging from 0.6488 m to 1.068 m are presented, since only seven times the bearing length (0.06 m) is designated for the thermal shaft, in order to improve computational efficiency, as mentioned in Sec. 3.

Compared with the aligned case, the journal high ΔT region is wider with respect to rpm for the misaligned case. The highest journal ΔT of the misaligned case reaches 9.88 °C. The high journal ΔT region occurs mainly in the rotor axial length from 0.8288 m to 0.8888 m which corresponds to the location of the fluid film bearing. Outside of this region shows relatively small journal ΔT values from 0 deg to 4 deg which justifies the thermal shaft length assumption.

The high journal ΔT induces increased thermal bow, decreased minimum film thickness ratio, and large vibrations as shown in Fig. 12(*b*). Large vibration levels are found at the rotor center (from 0.1 mm to 0.2 mm peak to peak), and the overhung end side (from 0.4 mm to 0.6 mm peak to peak). This distribution of the pk-pk vibration along the rotor axial direction is consistent with the mode shape in Fig. 9 which confirms the resonance of this bending mode.

Figures 13 and 14 show simulation results for the Rotor 2 case. A comparison of Figs. 11 and 13 show that the ME instability for the Rotor 1 aligned case is eliminated by increasing the bearing clearance from 68 μm for Rotor 1 to 84 μm for Rotor 2.

The amount of the bearing radial clearance change is realistic considering the manufacturing tolerances of the bearing and shaft.

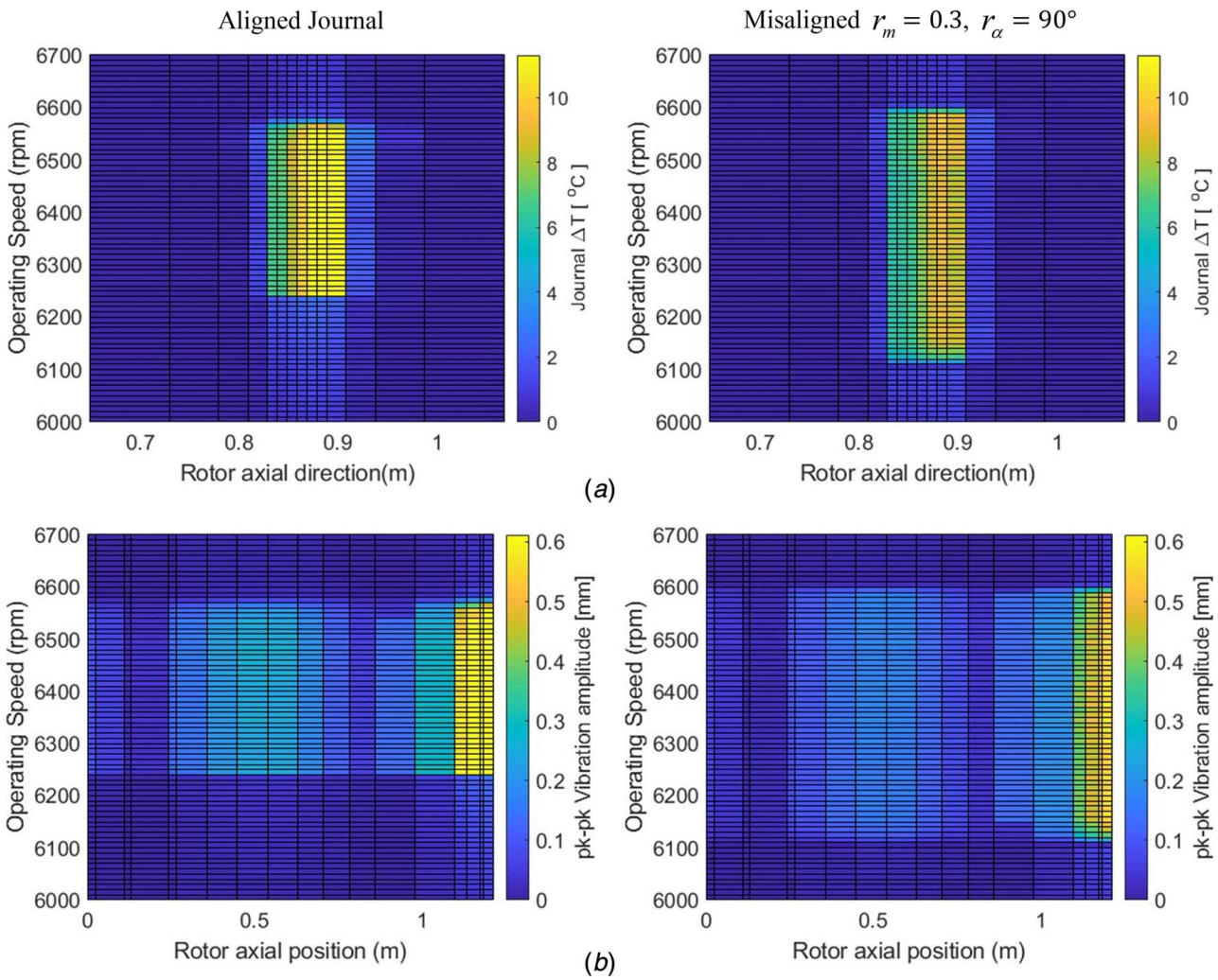

Fig. 12 Comparison of (*a*) peak journal ΔT and (*b*) pk-pk vibration amplitude versus rpm and axial position for the Rotor 1 case

Assuming the IT7 standard [27] for the shaft and bearing pad thickness, the manufacturing tolerances of the pad thickness and shaft diameter is ±0.018 mm and ±0.035 mm for pad thickness of 12 mm and the shaft diameter of 80 mm, respectively. Then, the maximum error in the bearing clearance can be up to ±0.0178 mm. The Rotor 2 linear model revealed that the third (bending) critical speed occurs at 6290 rpm which is about 50 rpm lower than that of the Rotor 1 case.

Figure 13(*a*) shows the no ME condition for the Rotor 2 aligned case becomes a severe ME condition for the misaligned bearing case. The ME synchronous instability leading to an unacceptable vibration level is observed from 6200 rpm to 6360 rpm. The 160 rpm ISR for the misaligned Rotor 2 case is less than the 430 rpm ISR for the misaligned Rotor 1 case. The increase in ISR between the aligned and misaligned states is nearly the same for Rotor 1 (140 rpm) and Rotor 2 (160 rpm).

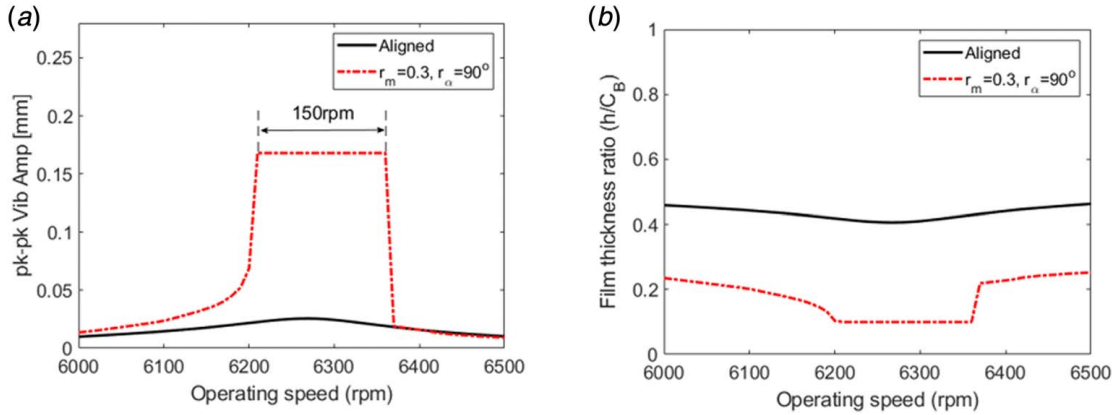

Fig. 13 Comparison of (*a*) pk-pk vibration at NDE bearing position and (*b*) minimum film thickness ratio for Rotor 2 case

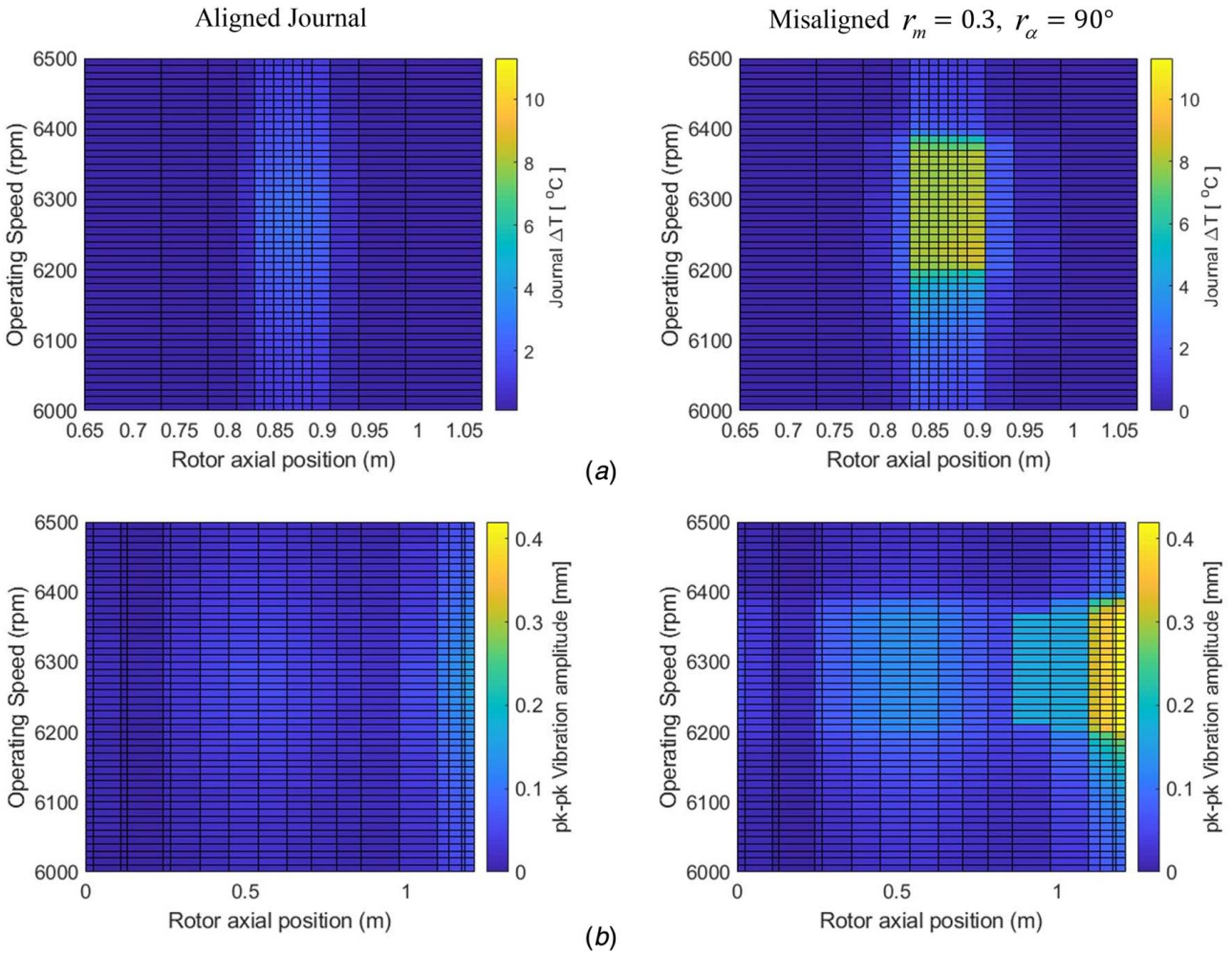

Fig. 14 Comparison of (*a*) peak journal ΔT and (*b*) pk-pk vibration amplitude versus rpm and axial position for the Rotor 2 case

Figure 14 shows a comparison of the pk-pk vibration and journal ΔT versus rpm and axial position, for the aligned and misaligned journal cases. The highest journal ΔT, 8.5 °C, and the highest vibration, up to twice C_B, are seen to occur near the third bending critical speeds of 6290 rpm. Similar to the Rotor 1 case, the vibration distribution level is most significant at the overhung end side, indicating the increased thermal bow at the overhung side, and the resultant ME instability.

Rotor 1 transient simulations were performed at 6120 rpm and 6570 rpm, as shown in Figs. 15 and 16. All parameter inputs of the rotor-bearing system are identical to the aforementioned steady-state simulation results. The misalignment ratio of 0.3 and the phase of 90 deg are again utilized for the misaligned journal case.

Figure 15(*a*) shows the 1× filtered polar plot at the NDE bearing location at 6120 rpm. The texts on the plot indicate the time (in minutes) when the vibration amplitude and the phase are measured. The misaligned journal produces a relatively large thermal spiral with time-varying pk-pk vibration amplitude. The phase angle with respect to the initial imbalance of the aligned case converges quickly, while that of the misaligned journal keeps varying from 0 deg to 360 deg during the entire simulation time. This result agrees with the steady-state results in Fig. 11 where the vibration of the misaligned does not converge with time, and the aligned case shows less vibration level.

Figure 15(*b*) shows that the misalignment effect increases the vibration level since the pk-pk vibration amplitudes of the misaligned case oscillate between 28.13 μm and 13.28 μm, while the response of the aligned journal decays to its steady-state vibration level of 8 μm. The misalignment gives rise to more asymmetric viscous heating in the journal caused by its decreased minimum film thickness.

Figure 15(*c*) shows that the misaligned journal has reduced the minimum film thickness ratio compared with the aligned case, although the area average (decreased) film thickness ratio of both cases is almost identical. The decreased mean film thickness was calculated by subtracting the thermal expansion of the shaft and pads from the nominal film thickness.

The minimum film thickness ratio of the misaligned journal fluctuates from 0.2 to 0.25, while the ratio of the aligned one is observed between 0.42 and 0.5. The impact of the pad-pivot stiffness and bearing radial clearance on the ME was investigated in Ref. [11], which showed that a softer pivot and increased bearing clearance tended to suppress ME. These parameter changes increased the minimum film thickness ratio, causing less viscous heating. Similarly, the decreased minimum film thickness due to the misaligned journal will produce more viscous heating in the journal surface area, especially where the journal is tilted. This may result in an increased shaft/bearing thermal expansion ratio and increased journal ΔT, exacerbating the ME.

The shape of the pk-pk journal surface temperature ΔT at the axial center of the bearing, as shown in Fig. 15(*d*) is similar to the vibration level in Fig. 15(*a*), which demonstrates the coupling between journal temperature and journal motions. The ME unstable vibration in the rotor system is governed by the journal ΔT and its resultant thermal bow amplitude, which is a unique feature of the ME.

Figure 16 shows the transient simulation results at the higher speed 6570 rpm. Figure 16(*a*) shows a diverging spiral shaped 1× polar plot for the misaligned case leading to the unacceptable

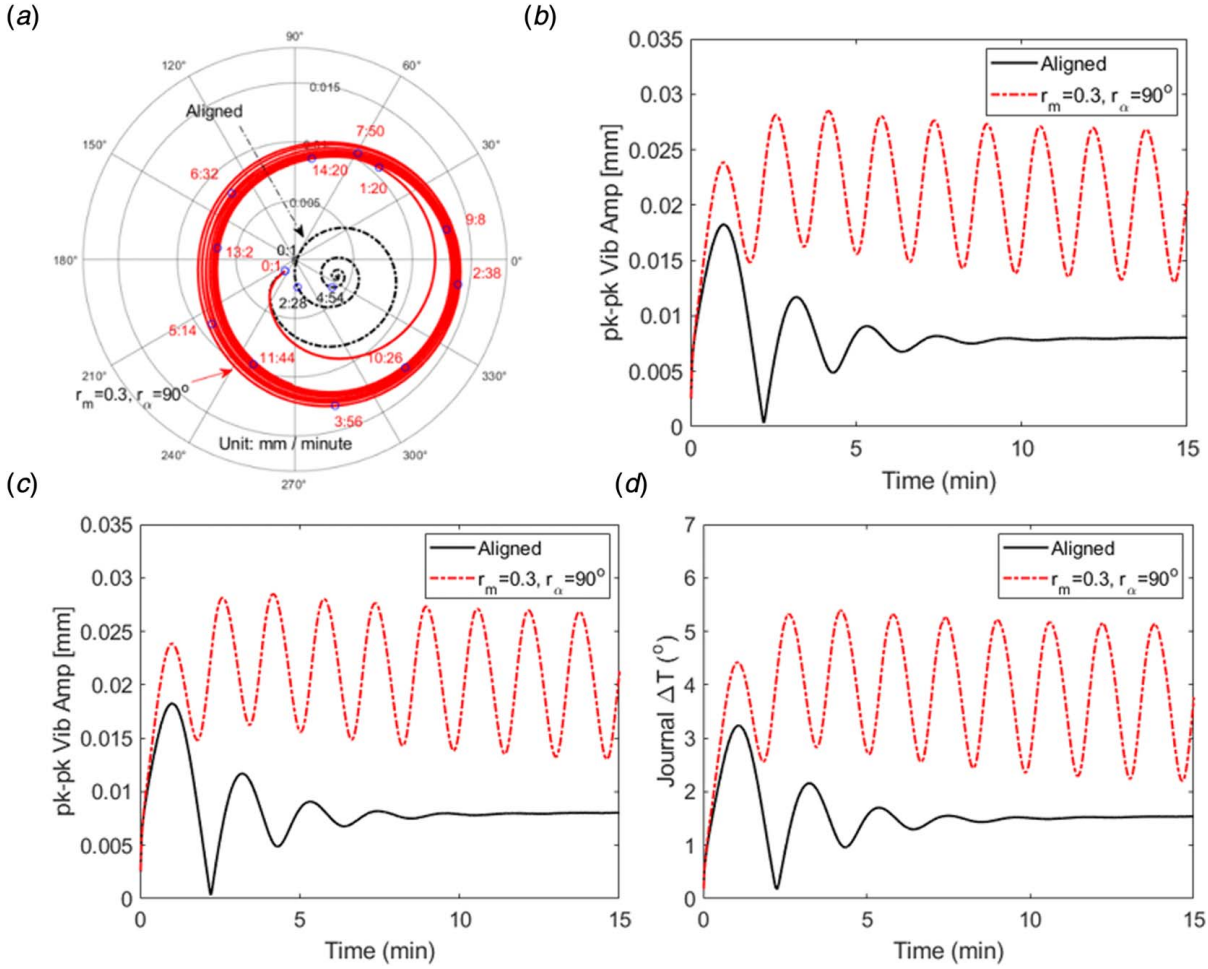

Fig. 15 Effects of misalignment on (*a*) 1× polar plot, (*b*) pk-pk vibration at NDE bearing position, (c) film thickness ratio, and (*d*) journal ΔT of Rotor 1 case at 6120 rpm

vibration level at 6 min 11 s, while the spiral of the aligned journal converges to its steady-state value. Figure 16(*b*) shows that the corresponding vibration amplitude, with an increasing trend up to 49 μm. The unacceptable vibration level occurs at that time and the journal ΔT of the misaligned case reaches 11 °C, which could cause a significant thermal bow. The aligned case results show acceptable levels of vibration, journal ΔT, and minimum film thickness ratio. The fast Fourier transform (FFT) of NDE bearing pk-pk vibration at 6570 rpm is shown in Figs. 16(*e*) and 16(*f*), which confirms that the ME vibration is synchronous.

Figure 17(*a*) illustrates how the high spot leads the hot spot for the misaligned journal case at 6570 rpm, and time equal to 6 min. The hot and high spots are seen to gradually move around the journal circumference as time increases.

Figure 17(*b*) shows that the phase lag of the hot spot behind the high spot is approximately 20 deg during most of the simulation time except the times where the phase lag drops then returns. These times correspond to the troughs in vibration amplitude in Fig. 16(*f*). In these instances, the synchronous vibration amplitude gets small so that the temperature asymmetry decreases. Figure 17(*c*) shows the corresponding journal surface temperature distribution at three different simulation times, including 1 min 1 s, 1 min 51 s, and 4 min 57 s. A major indicator of the ME is the spiral movement of the 1× phasor in the polar plot domain as shown in Fig. 16(*a*). Figure 17(*b*) shows that the hot spot lags the high spot, but the rotordynamics causes the high spot to follow the heavy spot (imbalance) that is caused by the thermal bow in the plane of the hot spot. Thus the high spot follows the hot spot which is always lagging the high spot. This feedback mechanism causes the spiral motion of the high spot 1× phasor in the polar plot.

The temperature distribution at the bearing mid-plane, the induced thermal bow, and the shaft thermal expansion ratio are shown in Fig. 18, for 6570 rpm, and aligned (left) and misaligned (right) cases. These results are measured at the end of each simulation time (15 min for the aligned, 6 min 17 s for the misaligned case). Figure 18(*a*) shows a maximum journal ΔT of 13°C in the misaligned case, while the isotherms of the aligned journal show a relatively concentric distribution. For the misaligned case, the hot spot is located at 22.7 deg, which lags about 10 deg behind the high spot location (32.8 deg).

The corresponding thermal bow due to the journal ΔT is shown in Fig. 18(*b*). The phase of the thermal bow at the rotor end is 247.7 deg for the aligned case, which is 185 deg away from the corresponding hot spot location (62.5 deg) while that of the misaligned journal is seen at 206.3 deg, and it is 183.6 deg away from its hot spot location. The amplitude of the thermal bow at the overhung end is 0.0344 mm with misalignment, which is about six times larger than that of the aligned case (0.0054 mm). This increases the synchronous excitation in the system. The thermal expansion of the shaft due to the viscous shearing is presented in Fig. 18(*c*). A relatively high expansion ratio (=0.22) is observed for the misaligned case at circumferential positions ranging from 0 deg to 90 deg, which corresponds to the high-temperature region and hot spot location in Fig. 18(*a*). Figure 18 shows the thermal expansion only in the rotor axial length matching the bearing location (from 0.8288 m to

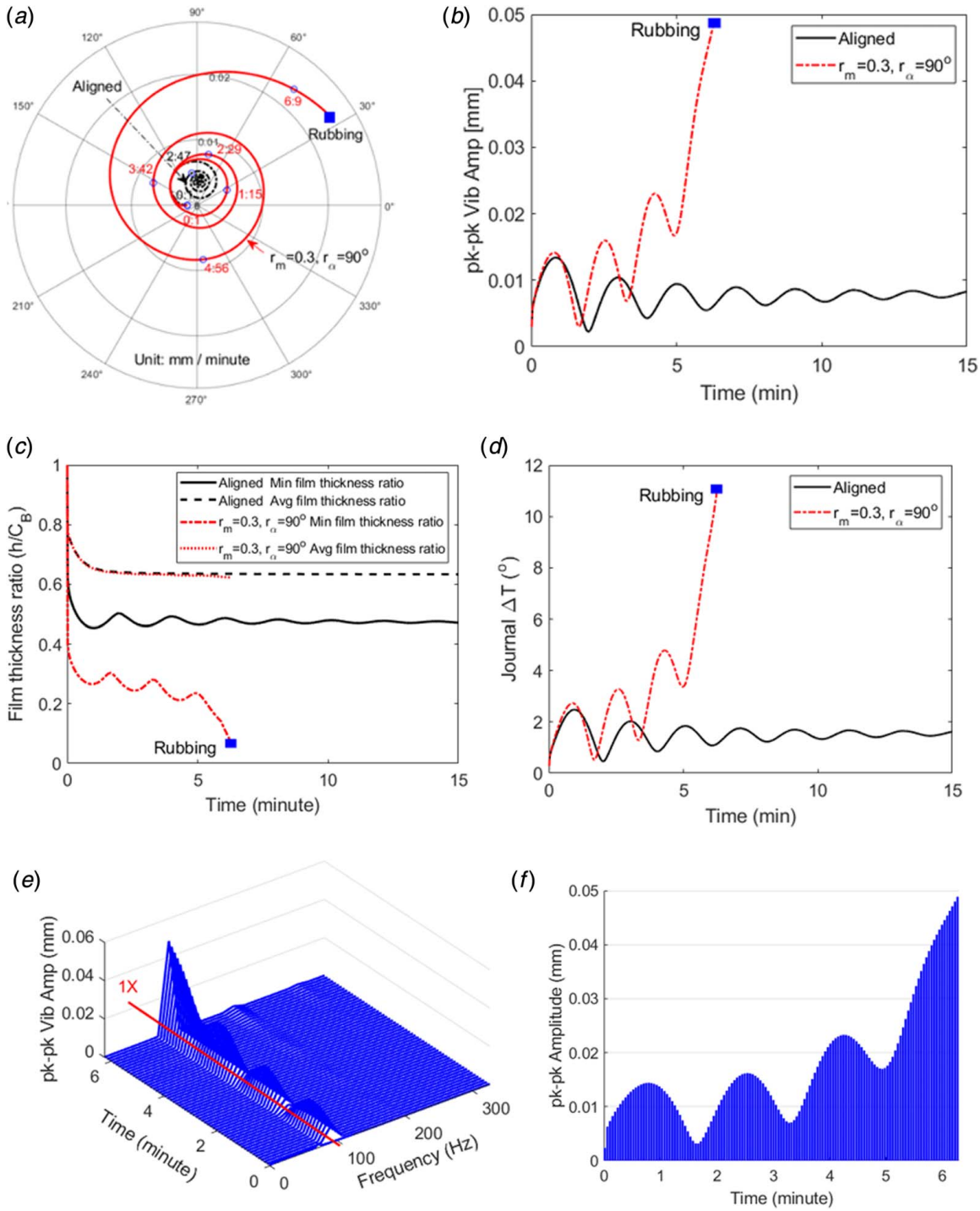

Fig. 16 Effect of misalignment on (*a*) 1× polar plot, (*b*) pk-pk vibration at NDE bearing position, (*c*) film thickness ratio, (*d*) journal ΔT, and (e) and (*f*) FFT of pk-pk vibration at NDE bearing position of Rotor 1 case at 6570 rpm

0.8888 m). The steady-state approach (Fig. 11) was validated by its good agreement with the transient approach for the Rotor 1 case at 6120 rpm and 6570 rpm, with and without the misalignment effect.

Figure 19 shows the film thickness ratio for the five pads at the end of the simulation time. The misaligned case shows an asymmetric distribution along the bearing axial direction while the aligned journal exhibits near symmetry. Figure 19(*b*) corresponds to the misaligned case with the 90 deg misalignment phase shown in Fig. 3(*a*), and the pad arrangement in Fig. 8. A large region has decreased film thickness at the NDE side in pads 1, 2, and 5, while the opposite trend is seen in the same pads at the DE side (a large region with increased film thickness). The damped unbalance response and damping ratio from the linear analysis showed only marginal impact due to misalignment. Therefore, the cause of the film thickness asymmetry along with the decreased minimum film thickness is attributed to the ME induced by the misaligned journal.

4.1 Effect of Misalignment Ratio. The effect of the misalignment ratio ($r_y = A_y/C_B$ in Fig. 2) on the ISR is investigated for both

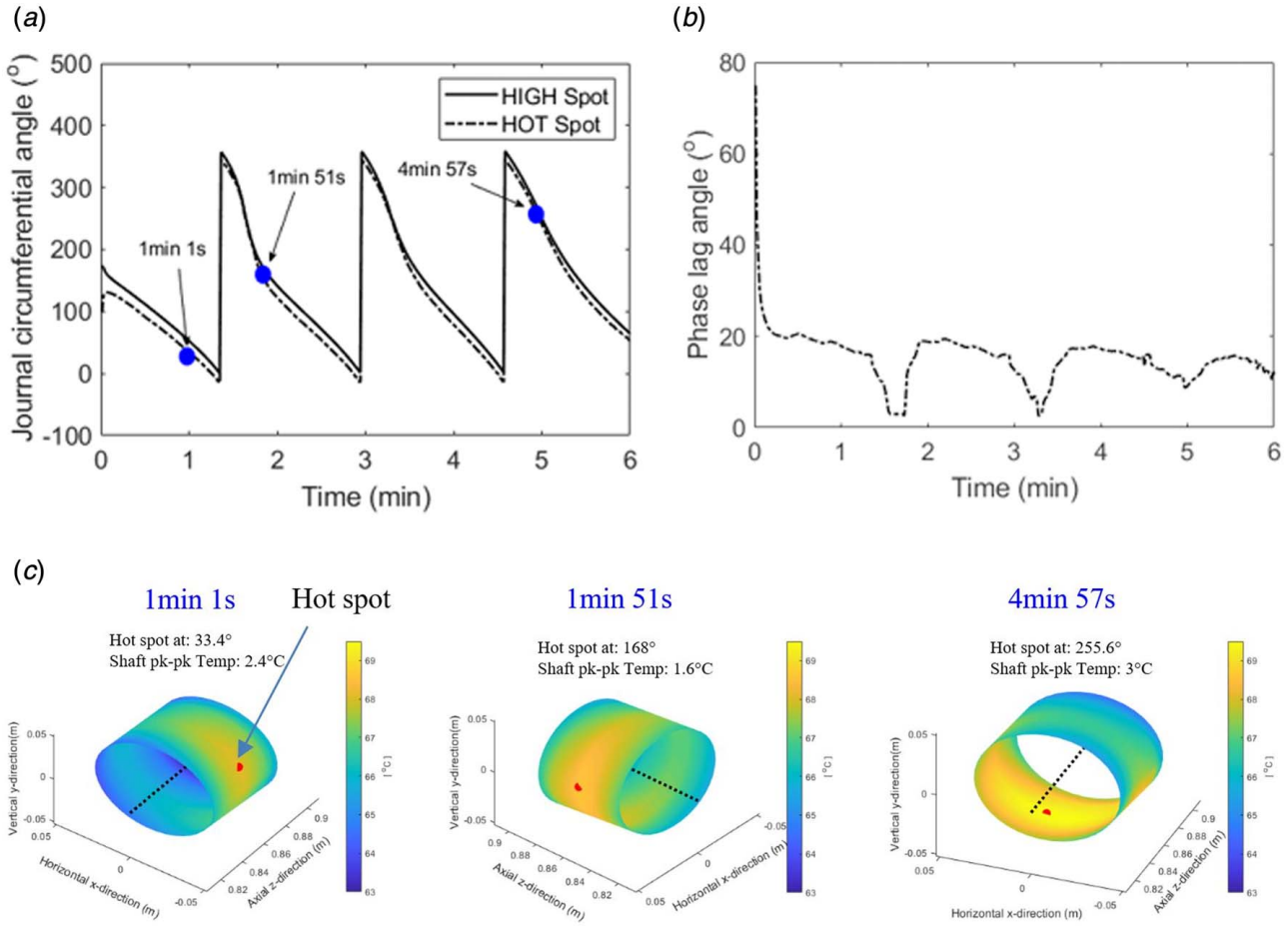

Fig. 17 Responses at 6750 rpm: (*a*) high and hot spot phase angles, (*b*) phase lag angle of hot spot behind high spot, and (*c*) journal surface temperature distribution at three different times

Rotor 1 and Rotor 2 cases, and the steady-state transient simulation results are presented in Fig. 20. The ratio of the misalignment ratio varied from 0 to 0.3 with an increment of 0.1, and the misalignment phase ($r_\alpha = \tan^{-1} \alpha_y/\alpha_x$ in Fig. 2) stays constant at 90 deg for all cases. All other parameter settings are identical with the aforementioned simulation results. The ISR due to the ME increases for both rotor cases as the misalignment ratio increases. The detailed ISR results are listed for different misalignment ratios in Table 2. In both rotor cases, the misalignment showed no significant effect when the misalignment ratio = 0.1, as the increase of the ISR is only 10 rpm for Rotor 1, and no ME is induced in Rotor 2. The misalignment effect on the ME becomes more evident when the misalignment ratio increases above 0.2. Table 2 shows an increase in ISR by 100 rpm and 140 rpm compared with that of the aligned journal for Rotor 1, when $r_m = 0.2$ and 0.3. For Rotor 2, the ME is first seen to occur with $r_m = 0.2$, and its ISR is small at 80 rpm. The maximum ISR of the Rotor 2 is 160 rpm when the misaligned ratio is further increased to $r_m = 0.3$. Increases of the ISR for Rotor 2 case are 80 rpm for $r_m = 0.2$ and 160 rpm for $r_m = 0.1$, respectively. The increased ISR with $r_m = 0.2$and 0.3 for both Rotor 1 (100 rpm and 140 rpm) and Rotor 2 (80 rpm and 160 rpm) cases are similar, indicating the bearing radial clearance does not have a significant impact on the misalignment-induced ME. These results demonstrate that the misaligned journal induces more severe ME when its misalignment ratio exceeds a certain level ($r_m > 0.2$ in this case).

The corresponding pk-pk vibration amplitude and the pk-pk shaft temperature distribution along the rotor axial direction for Rotor 2 is illustrated in Fig. 21. As expected, high pk-pk temperature and vibration are observed in the wider ISR as the misalignment ratio increases.

Transient simulations of Rotor 1 were conducted at 6570 rpm to validate the steady-state simulation results, as shown in Fig. 22. The unacceptable vibration level occurs only with $r_m = 0.2$ and 0.3 in Fig. 22(*a*), which agrees with the steady-state results in Fig. 20. The unacceptable vibration level occurs about 4 min faster with $r_m = 0.3$, compared with $r_m = 0.2$. High vibration levels at the NDE bearing location are observed for the two misaligned cases ($r_m = 0.2$ and 0.3) in Fig. 22(*b*). Although an unacceptable vibration level is not observed with $r_m = 0.1$, oscillating vibration with varying phase exists while the aligned case shows converging response to its steady-state position. The corresponding thermal bow amplitude and the phase of the rotor measured from the bearing node to the rotor end node are presented in Fig. 22(*c*). The thermal bow of the aligned case is 0.0056 m in magnitude and 247.7 deg in phase at the rotor end, while 0.0083 m and 211.2 deg for $r_m = 0.1$, 0.031 m, and 289.4 deg for $r_m = 0.2$, and 0.0313 m, and 206.57 deg for $r_m = 0.3$, at the rotor end.

The 1x polar plots for $r_m = 0.1$–0.3 are shown in Figs. 22(*d*)–22(*f*). The spiral with $r_m = 0.1$, which is marginally stable with non-diverging vibration response, changes to diverging shapes with increased misalignment ratios of 0.2 and 0.3. The time to reach 10% of C_b is 9 min 16 s for $r_m = 0.2$ and 6 min 10 s for $r_m = 0.3$. This indicates increased ME severity with increased misalignment ratio.

4.2 Effect of Different Pad-Pivot Types. The previously presented models and simulations utilized a cylindrical pad-pivot type which has only pad-tilting motions. The following results compare the effect of including a spherical pad pivot with rolling, yawing, and tilting motions. All other rotor and bearing parameters and

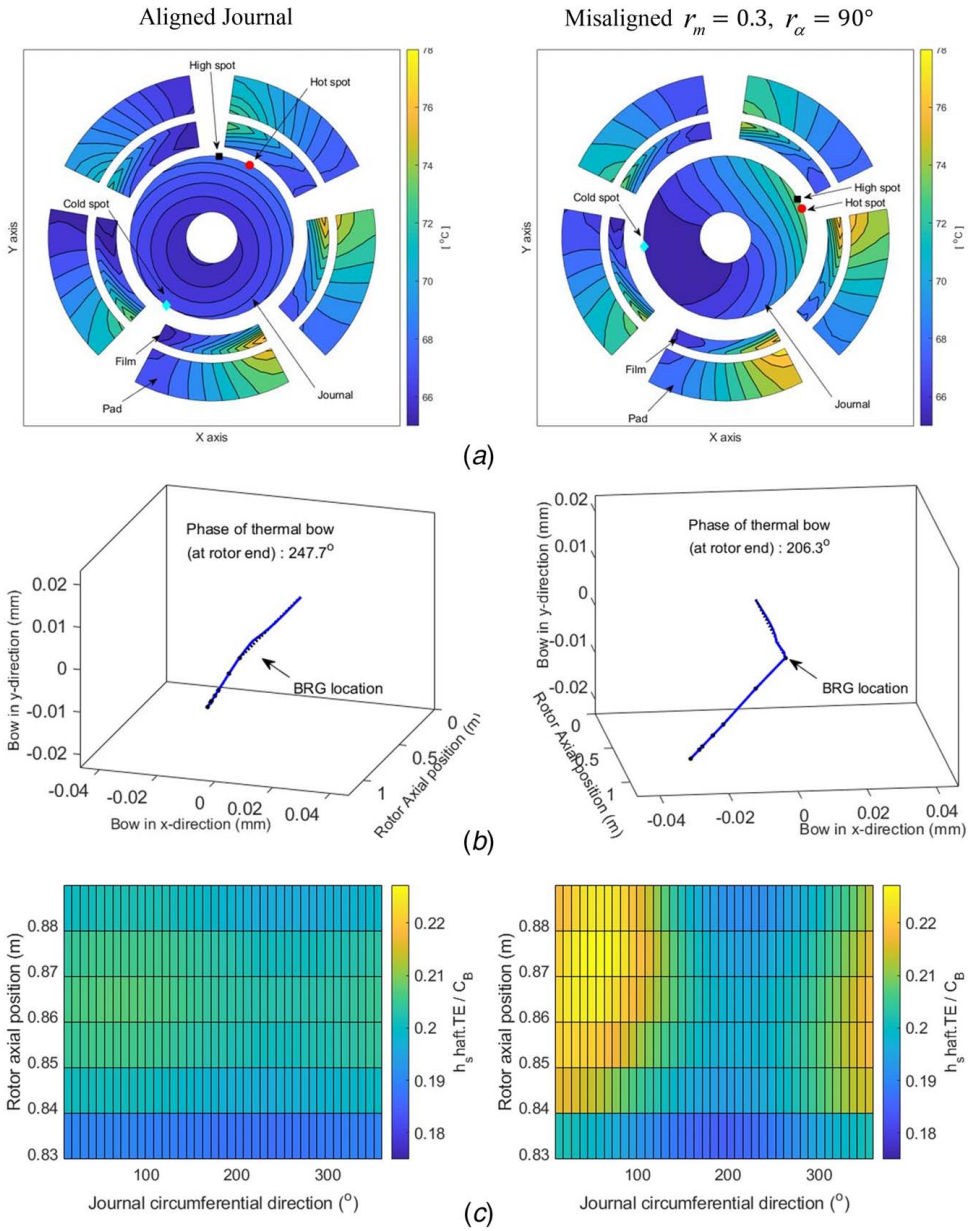

Fig. 18 Comparison of (*a*) temperature distribution at bearing mid-plane, (*b*) thermal bow, and (c) shaft thermal expansion ratio at 6570 rpm for the aligned (left) and misaligned (right) cases

operating conditions are the same as for the previous models and simulations. Figure 23 shows steady-state vibration level and journal ΔT results for the spherical pad-pivot model, performed with different misalignment ratios including $r_m = 0$ (aligned journal) and $r_m = 0.3$, $r_\alpha = 90$ deg (misaligned journal). The speed ranges of the high vibration and temperature of the aligned case are found from 6250 rpm to 6550 rpm, which is almost identical to the aligned case for the cylindrical pivot type. The ISR for the misaligned case ($r_m = 0.3$, $r_\alpha = 90$ deg) does not change from the aligned case. The increase of ISR with the same misalignment ratio was 160 rpm for the cylindrical pad-pivot type. This indicates that the additional pad motions (rolling) of the spherical pad-pivot compensates the misalignment effect on the rotor-bearing system.

The transient simulation was conducted at 6570 rpm for both pad-pivot types with different misalignment ratios including $r_m = 0$ (aligned journal) and $r_m = 0.3$, $r_\alpha = 90$ deg (misaligned journal). The journal ΔT and the 1× vibration polar plot results are shown in Fig. 24 for both pivot types. Note that in the cylindrical pad-pivot case, the misaligned ratio of $r_m = 0.3$, $r_\alpha = 90$ deg induces a severe ME leading to the unacceptable vibration level as shown in the journal ΔT and polar plots. In comparison, the spherical pivot model results show almost identical stable journal ΔT and vibration amplitude/phase levels, regardless of the misalignment ratio.

Figures 25(*a*) and 25(*b*) show the rolling motions of the spherical pad-pivot at 6570 rpm for different misalignment ratios. The steady-state angular displacements of the five pad motions are relatively small for the perfectly aligned journal model. However, with the misalignment ratio ($r_m = 0.3$, $r_\alpha = 90$ deg), the steady-state positions of all five pads have been significantly displaced as shown in Fig. 25(*b*). The increased rolling movements are more evident in pad 1, 3, and 4 than other pads, where the pad locations are shown in Figs. 3 and 8. The tilted journal (with misalignment phase of 90 deg) affects the minimum film thickness significantly. The corresponding film thickness ratio of pads with the misalignment effect is shown in Fig. 25(*c*). Compared with the misaligned case equipped with the cylindrical pivot in Fig. 19(*c*), no film thickness asymmetry is seen to occur in the figure, indicating the compensated misalignment effect from the spherical pivot motions. This result verifies that the misalignment-induced ME can be avoided by suppressing

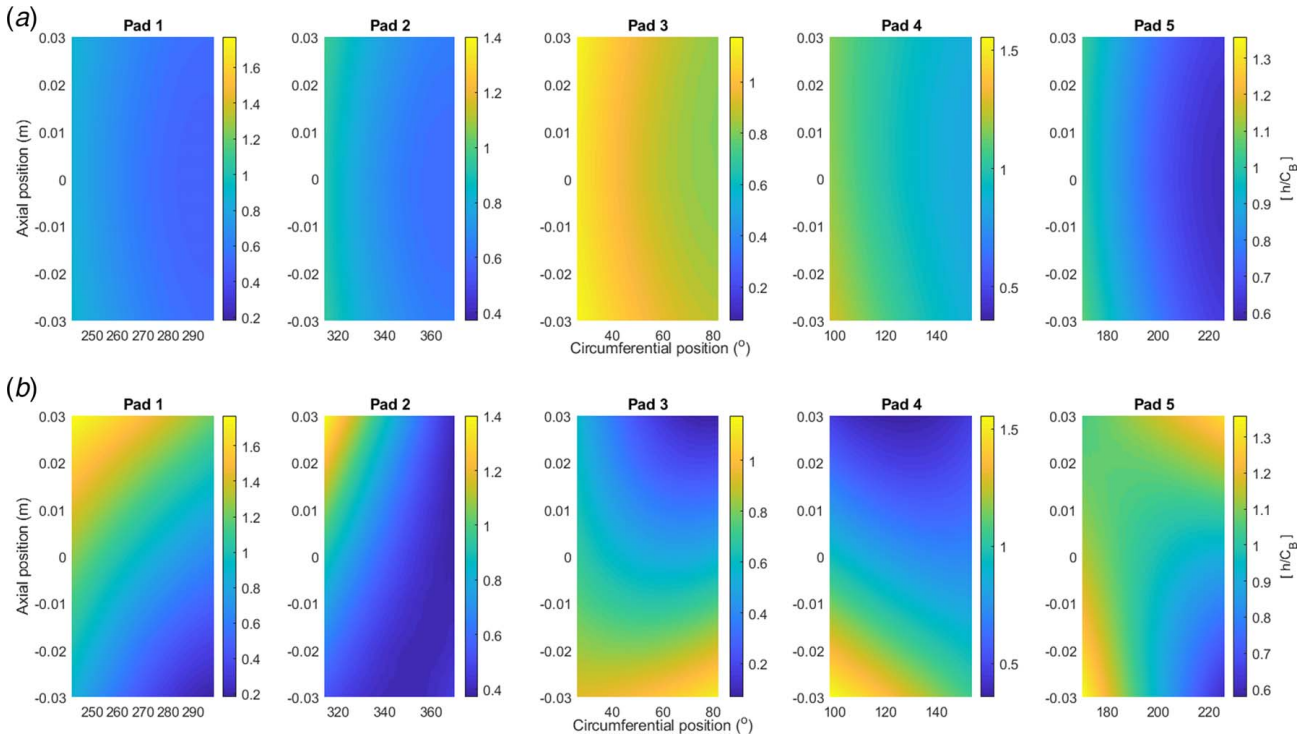

Fig. 19 Pad film thickness distribution at 6570 rpm: (*a*) aligned journal and (*b*) misaligned $r_m = 0.3$, $r_\alpha = 90$ deg

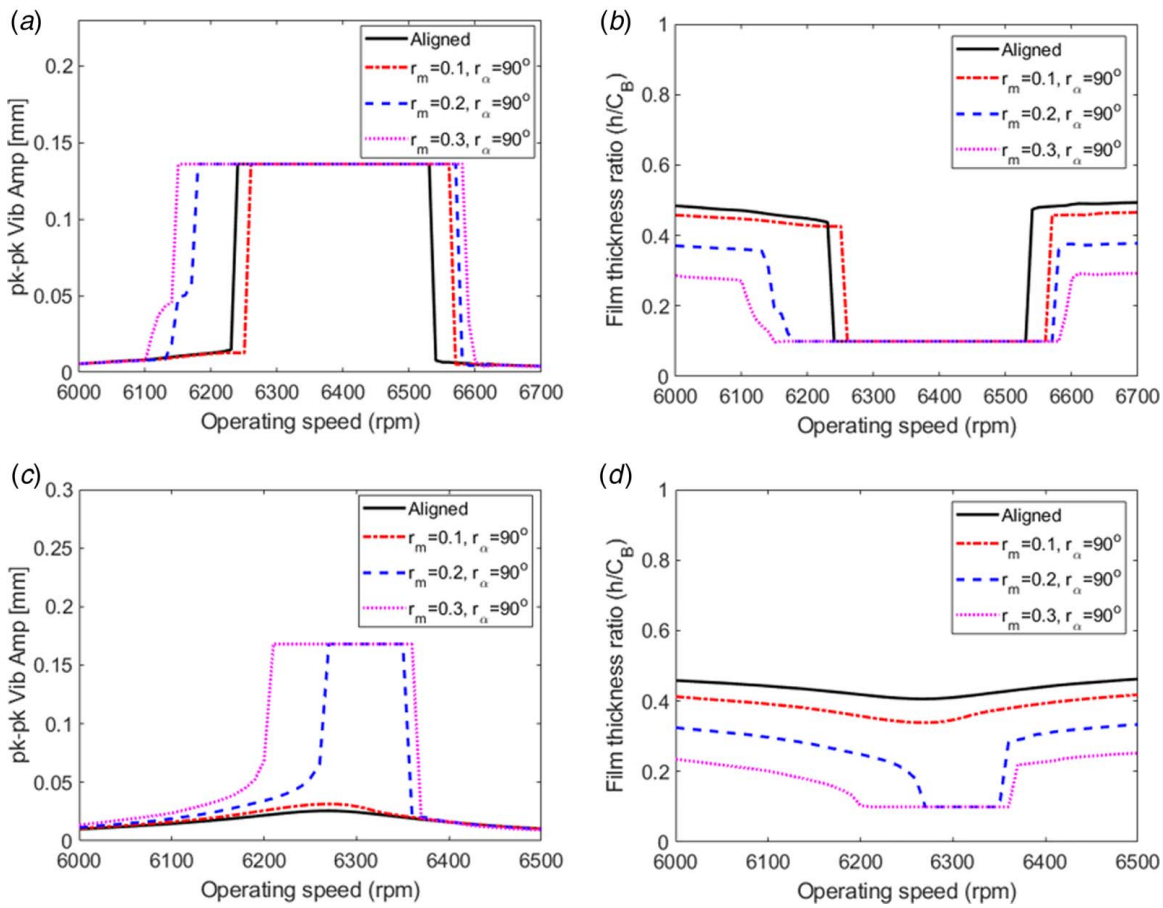

Fig. 20 Comparison of (*a*) pk-pk vibration at NDE bearing position of Rotor 1, (*b*) minimum film thickness ratio of Rotor 1, (*c*) pk-pk vibration at NDE bearing position of Rotor 2, and (*d*) minimum film thickness ratio of Rotor 2 with different misalignment ratio

Table 2 ISR with different misalignment ratio ($r_m = \sqrt{r_x^2 + r_y^2}$ in Fig. 2)

	Aligned	$r_m = 0.1$, $r_\alpha = 90$ deg	$r_m = 0.2$, $r_\alpha = 90$ deg	$r_m = 0.3$, $r_\alpha = 90$ deg
Rotor 1	6240–6530 rpm (290 rpm)	6260–6560 rpm (300 rpm)	6180–6570 rpm (390 rpm)	6150–6580 rpm (430 rpm)
Rotor 2	No Morton (0 rpm)	No Morton (0 rpm)	6270–6350 rpm (80 rpm)	6200–6360 rpm (160 rpm)

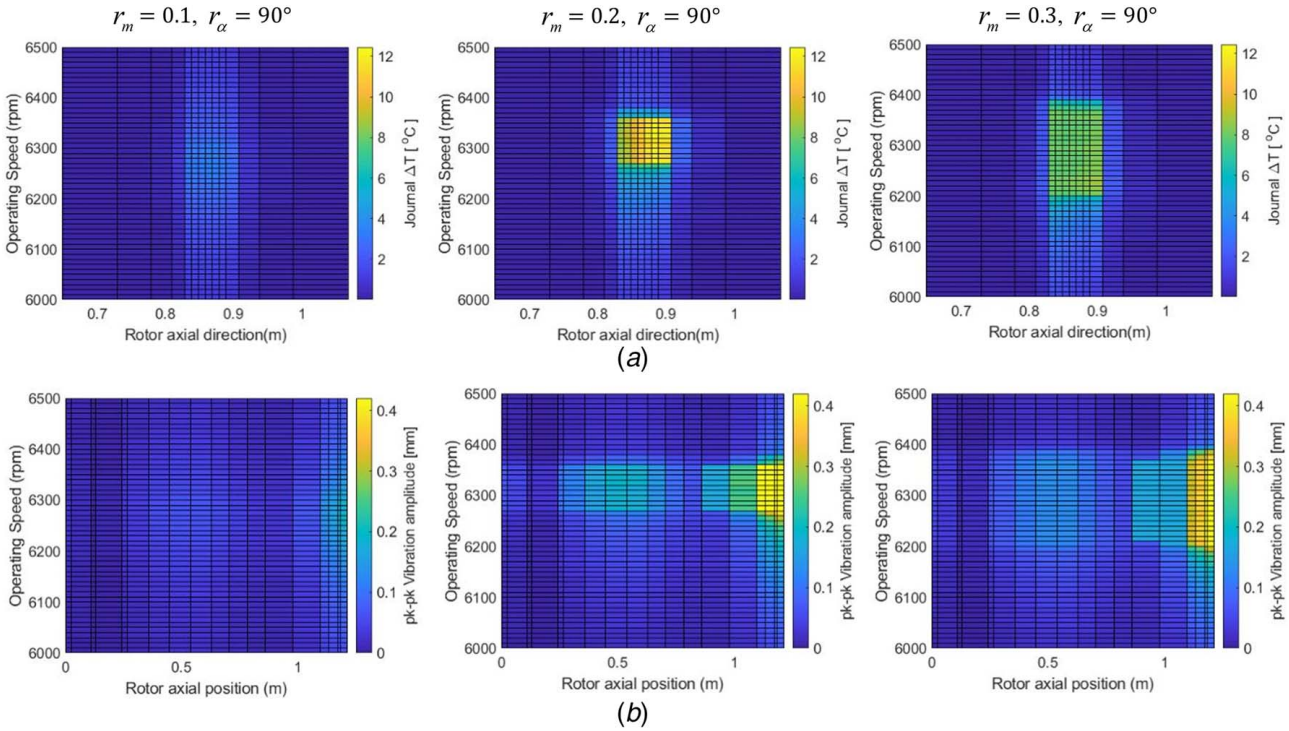

Fig. 21 Comparison of (*a*) peak journal ΔT and (*b*) minimum film thickness ratio across rotor axial positions for Rotor case 2 with different misalignment ratios

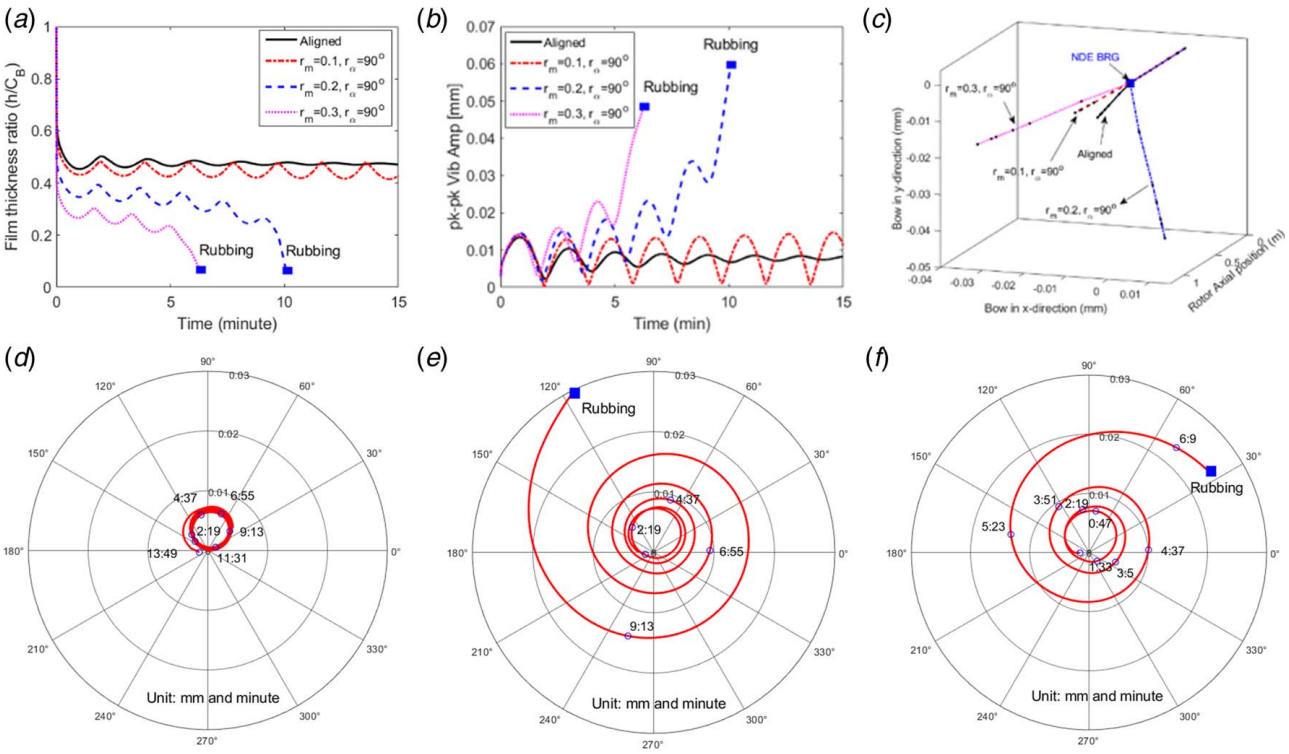

Fig. 22 Comparison of (*a*) film thickness ratio of Rotor 1, (*b*) pk-pk vibration at NDE bearing position of Rotor 1, (*c*) thermal bow of Rotor 1, (*d*) 1× polar plot with $r_m = 0.1$, $r_\alpha = 90$ deg, (*e*) 1× polar plot with $r_m = 0.2$, $r_\alpha = 90$ deg, and (*f*) 1× polar plot with $r_m = 0.3$, $r_\alpha = 90$ deg at 6570 rpm

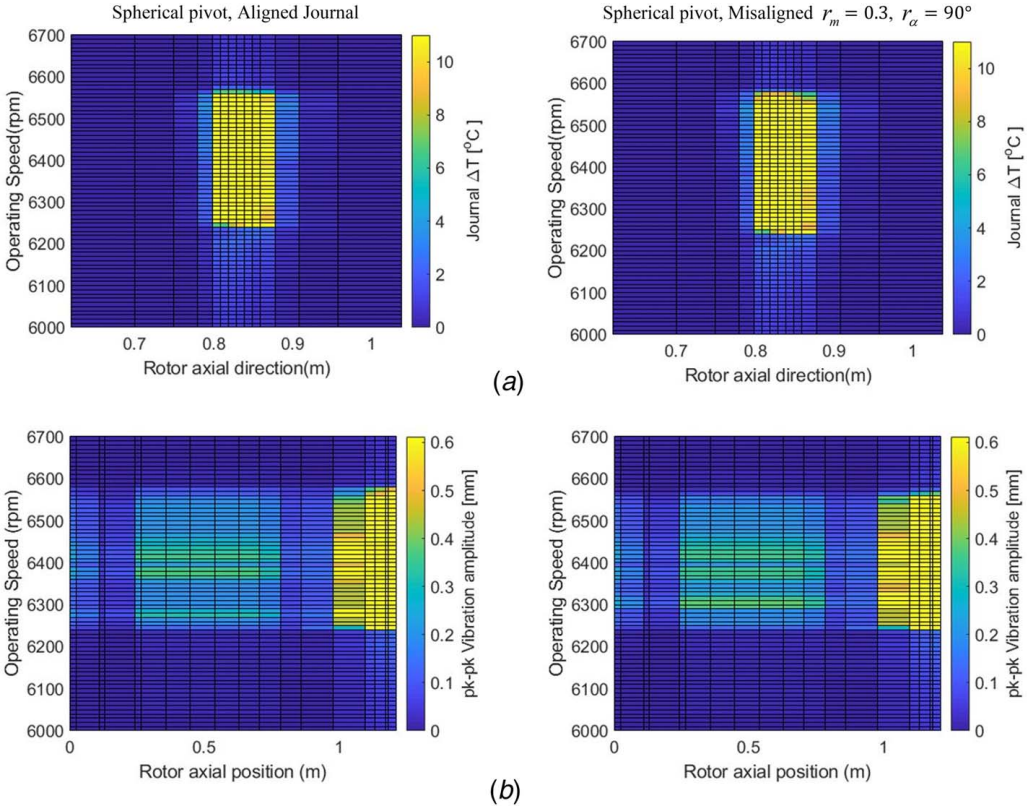

Fig. 23 Comparison of (*a*) peak journal ΔT and (*b*) pk-pk vibration amplitude for aligned and misaligned journals, for Rotor 1 with spherical pad-pivot model

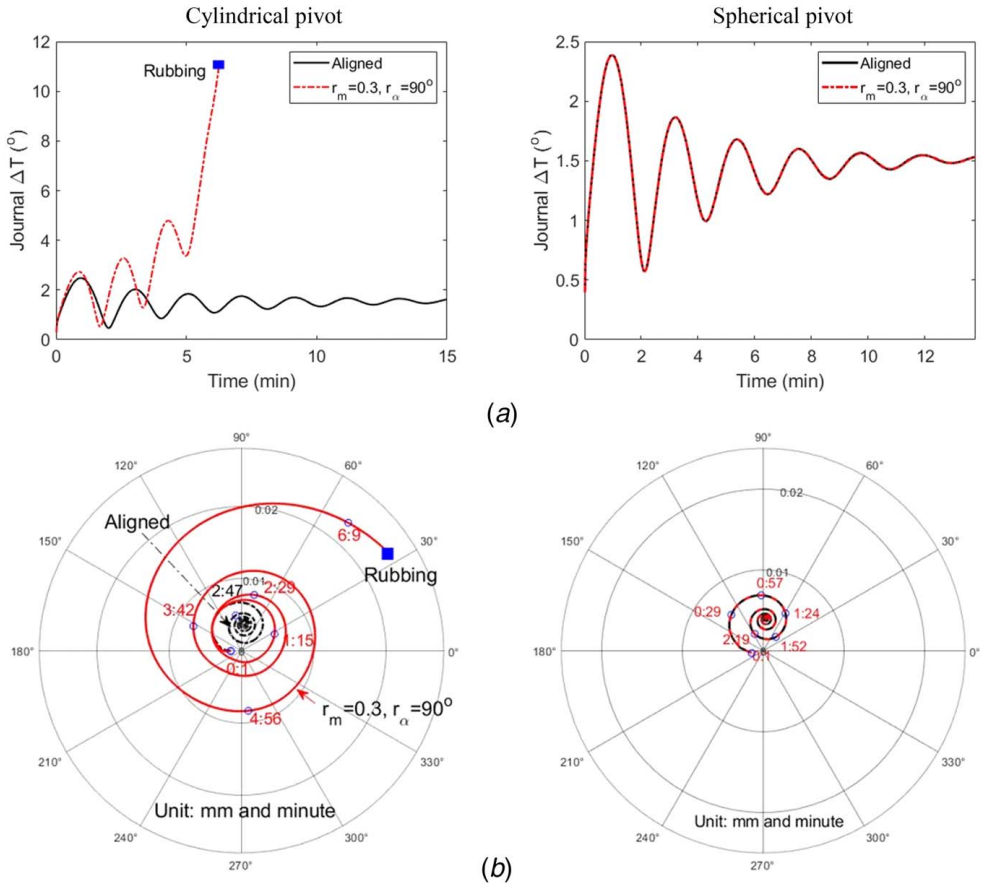

Fig. 24 Comparison of cylindrical and spherical pivot model: (*a*) peak journal ΔT and (*b*) pk-pk 1× vibration polar plot of Rotor 1 case, at 6570 rpm

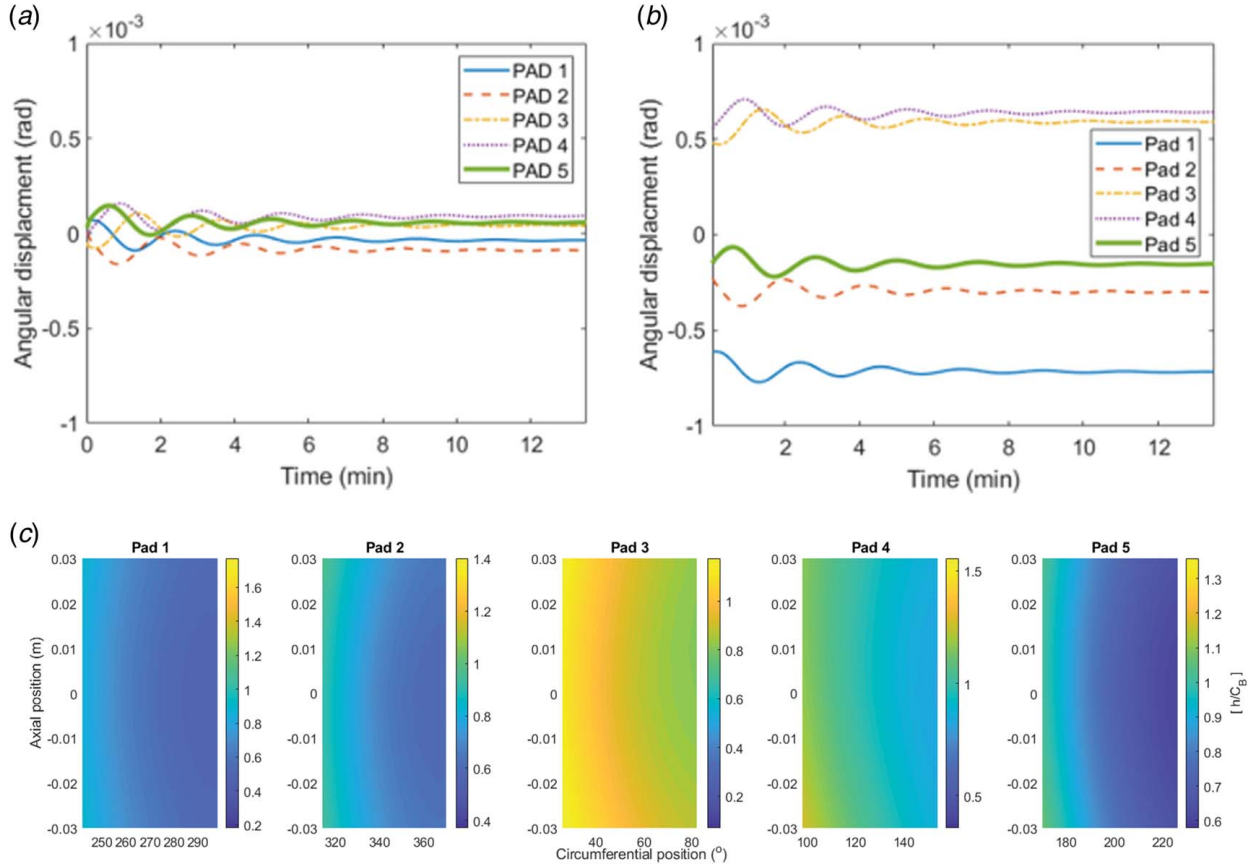

Fig. 25 Comparison of pad rolling motions of spherical pivot-type model for (*a*) aligned journal, (*b*) misaligned journal (r_m = 0.3, r_α = 90 deg), and (c) film thickness distribution of misaligned journal r_m = 0.3, r_α = 90 deg of Rotor 1 case at 6570 rpm

the film asymmetry with the spherical pivot and also demonstrates that the film asymmetry is the one potential root cause of the misalignment-induced ME.

5 Conclusions

This paper presents results of a study for the effects of bearing misalignment on the ME, utilizing high-fidelity rotordynamics and thermodynamics models, based on the 3D FEM. The following conclusions are made: (1) journal misalignment induces decreased film thickness and film thickness distribution asymmetry which increases the ME ISR. Simulations for two rotor cases with different bearing clearances showed that the ISR was nearly invariant with respect to bearing radial clearance. It was also demonstrated that a rotor operating free from the ME may experience a ME instability if the journal becomes misaligned. (2) Severe ME instability was observed to occur when the misalignment ratio exceeded a certain amplitude ($r_m > 0.2$). High misalignment ratios ($r_m = 0.2$ and 0.3) expanded the ME instability speed range and increased the ME severity. (3) Spherical pad-type pivot compensated the misalignment effect, as confirmed by the invariance of the ISR with misalignment ratio increase when spherical pivot models were included. The compensation effect was confirmed with the increased angular displacements of the pad rolling motions in accordance with the misalignment direction.

Acknowledgment

The authors gratefully acknowledge support of this research from the Texas A&M Turbomachinery Research Consortium (TRC) members companies.

Conflict of Interest

There are no conflicts of interest.

Nomenclature

c = specific heat capacity of fluid film
k = thermal conductivity of fluid film
u = circumferential velocity of fluid film
v = axial velocity of fluid film
z = axial coordinate of the fluid film bearing
L = bearing length
R = journal radius
T = fluid film temperature
U = state vector of a rotor system
$h_{pad.TE}$ = thermal expansion of a pad
$h_{shaft.TE}$ = thermal expansion of a shaft
r_α = journal misalignment phase
y_{pvt} = pad-pivot deformation
A_x = journal end displacement in x direction
A_y = journal end displacement in y direction
C_1 = constants related to variable viscosity term
C_2 = constants related to variable viscosity term
C_b = bearing radial clearance
C_p = pad radial clearance
C_{ro} = damping matrix of a rotor system
$D_{\Delta T}$ = nodal displacement vector
F_{pad_i} = fluid film force from a ith pad
$F_{\Delta T}$ = thermal load vector
I_{roll_i} = roll inertia of a ith pad
I_{tilt_i} = tilting inertia of a ith pad
I_{yaw_i} = yaw inertia of a ith pad
K_{ro} = stiffness matrix of a rotor system

M_{pad_i} = mass of a ith pad
M_{ro} = mass matrix of a rotor system
T_0 = reference temperature
$\hat{e}_x$ = eccentricity in x direction
$\hat{e}_y$ = eccentricity in y direction
MO_{pitch_i} = rolling moment from a ith pad
MO_{tilt_i} = tilting moment from a ith pad
MO_{yaw_i} = yawing moment from a ith pad
α = coefficient of viscosity
α_{roll} = pad rolling angular displacement
α_x = misalignment angle in x direction
α_y = misalignment angle in y direction
β_{yaw} = pad yawing angular displacement
δ_{tilt} = pad tilting angular displacement
θ = circumferential coordinate of a bearing
θ_p = pad-pivot angular position
μ = variable viscosity
μ_0 = reference viscosity
ρ = density of fluid film

References

[1] Tong, X., Palazzolo, A., and Suh, J., 2017, "A Review of the Rotordynamic Thermally Induced Synchronous Instability (Morton) Effect," ASME Appl. Mech. Rev., **69**(6), p. 060801.
[2] de Jongh, F., and Van Der Hoeven, P., eds., 1998, "Application of a Heat Barrier Sleeve to Prevent Synchronous Rotor Instability," 27th Turbomachinery Symposium, Houston, TX, Sept. 20–24, pp. 17–26.
[3] Keogh, P., and Morton, P., 1994, "The Dynamic Nature of Rotor Thermal Bending Due to Unsteady Lubricant Shearing Within a Bearing," Proc. R. Soc. London, Ser. A, **445**(1924), pp. 273–290.
[4] Lee, J., and Palazzolo, A., 2012, "Morton Effect Cyclic Vibration Amplitude Determination for Tilt Pad Bearing Supported Machinery," ASME J. Tribol., **135**(1), p. 011701.
[5] Suh, J., and Palazzolo, A., 2015, "Three-Dimensional Dynamic Model of TEHD Tilting-Pad Journal Bearing–Part I: Theoretical Modeling," ASME J. Tribol., **137**(4), p. 041703.
[6] Suh, J., and Palazzolo, A., 2015, "Three-Dimensional Dynamic Model of TEHD Tilting-Pad Journal Bearing—Part II: Parametric Studies," ASME J. Tribol., **137**(4), p. 041704.
[7] Suh, J., and Palazzolo, A., 2014, "Three-Dimensional Thermohydrodynamic Morton Effect Simulation—Part I: Theoretical Model," ASME J. Tribol., **136**(3), p. 031706.
[8] Suh, J., and Palazzolo, A., 2014, "Three-Dimensional Thermohydrodynamic Morton Effect Analysis—Part II: Parametric Studies," ASME J. Tribol., **136**(3), p. 031707.
[9] Tong, X., Palazzolo, A., and Suh, J., 2016, "Rotordynamic Morton Effect Simulation With Transient, Thermal Shaft Bow," ASME J. Tribol., **138**(3), p. 031705.
[10] Tong, X., and Palazzolo, A., 2016, "Double Overhung Disk and Parameter Effect on Rotordynamic Synchronous Instability—Morton Effect—Part I: Theory and Modeling Approach," ASME J. Tribol., **139**(1), p. 011705.
[11] Tong, X., and Palazzolo, A., 2016, "Double Overhung Disk and Parameter Effect on Rotordynamic Synchronous Instability—Morton Effect—Part II: Occurrence and Prevention," ASME J. Tribol., **139**(1), p. 011706.
[12] Tong, X., and Palazzolo, A., 2017, "Measurement and Prediction of the Journal Circumferential Temperature Distribution for the Rotordynamic Morton Effect," ASME J. Tribol., **140**(3), p. 031702.
[13] Tong, X., and Palazzolo, A., 2018, "Tilting Pad Gas Bearing Induced Thermal Bowrotor Instability," Tribol. Int., **121**, pp. 269–279.
[14] Bouyer, J., and Fillon, M., 2002, "An Experimental Analysis of Misalignment Effects on Hydrodynamic Plain Journal Bearing Performances," ASME J. Tribol., **124**(2), pp. 313–319.
[15] Sun, J., and Gui, C. L., 2004, "Hydrodynamic Lubrication Analysis of Journal Bearing Considering Misalignment Caused by Shaft Deformation," Tribol. Int., **37**(10), pp. 841–848.
[16] El-Butch, A. M., and Ashour, N. M., 2005, "Transient Analysis of Misaligned Elastic Tilting Pad Journal Bearing," Tribol. Int., **38**(1), pp. 41–48.
[17] Sun, J., Deng, M., Fu, Y., and Gui, C., 2010, "Thermohydrodynamic Lubrication Analysis of Misaligned Plain Journal Bearing With Rough Surface," ASME J. Tribol., **132**(1), p. 011704.
[18] Xu, G., Zhou, J., Geng, H., Lu, M., Yang, L., and Yu, L., 2015, "Research on the Static and Dynamic Characteristics of Misaligned Journal Bearing Considering the Turbulent and Thermohydrodynamic Effects," ASME J. Tribol., **137**(2), p. 024504.
[19] Suh, J., and Choi, Y., 2016, "Pivot Design and Angular Misalignment Effects on Tilting Pad Journal Bearing Characteristics: Four Pads for Load on Pad Configuration," Tribol. Int., **102**, pp. 580–599.
[20] Das, S., Guha, S. K., and Chattopadhyay, A. K., 2002, "On the Steady-State Performance of Misaligned Hydrodynamic Journal Bearings Lubricated With Micropolar Fluids," Tribol. Int., **35**(4), pp. 201–210.
[21] Ebrat, O., Mourelatos, Z. P., Vlahopoulos, N., and Vaidyanathan, K., 2004, "Calculation of Journal Bearing Dynamic Characteristics Including Journal Misalignment and Bearing Structural Deformation," Tribol. Trans., **47**(1), pp. 94–102.
[22] Ahmed, A. M., and El-Shafei, A., 2008, "Effect of Misalignment on the Characteristics of Journal Bearings," ASME J. Eng. Gas Turbines Power, **130**(4), p. 042501.
[23] Lee, D., Sun, K., Kim, B., and Kang, D., 2017, "Thermal Behavior of a Worn Tilting Pad Journal Bearing: Thermohydrodynamic Analysis and Pad Temperature Measurement," Tribol. Trans., **61**(6), pp. 1074–1083.
[24] Sim, K., and Kim, D., 2008, "Thermohydrodynamic Analysis of Compliant Flexure Pivot Tilting Pad Gas Bearings," ASME J. Eng. Gas Turbines Power, **130**(3), p. 032502.
[25] Khonsari, M. M., and Booser, E. R., 2017, *Applied Tribology: Bearing Design and Lubrication*, John Wiley & Sons, New York.
[26] Heinrich, J., Huyakorn, P., Zienkiewicz, O., and Mitchell, A., 1977, "An 'Upwind' Finite Element Scheme for Two-Dimensional Convective Transport Equation," Int. J. Numer. Methods Eng., **11**(1), pp. 131–143.
[27] ISO, 2010, *Geometrical Product Specifications (GPS)-ISO Code System for Tolerances on Linear Size—Part 1: Basis of Tolerances, Deviations and Fits*, International Organization for Standardization, Geneva, Switzerland.